Actomyosin-II facilitates long-range retrograde transport of large cargoes by controlling axonal radial contractility

Tong Wang[1,3,*], Wei Li[1], Sally Martin[1,2], Andreas Papadopulos[1], Golnoosh Shamsollahi[1], Vanessa Lanoue[1], Pranesh Padmanabhan[1], He Huang[1], Xiaojun Yu[1], Victor Anggono[1,3] and Frederic A. Meunier[1,3,*]

Affiliations:

[1]Clem Jones Centre for Ageing Dementia Research, Queensland Brain Institute, The University of Queensland, Brisbane, QLD 4072, Australia.

[2]Current address: The Australian Institute for Bioengineering and Nanotechnology, The University of Queensland, Brisbane, QLD 4072, Australia.

[3]Senior author.

*Correspondence to: Tong Wang (t.wang4@uq.edu.au), or Frederic A. Meunier (f.meunier@uq.edu.au), Clem Jones Centre for Ageing Dementia Research, Queensland Brain Institute, The University of Queensland, Brisbane, Queensland 4072, Australia.

Abstract

Most mammalian neurons have a narrow axon, which constrains the passage of large cargoes such as autophagosome as they can be larger than the axon diameter. Variations in tension must therefore occur radially to facilitate changes in axonal diameter and ensure efficient axoplasmic trafficking. Here, we reveal that the transit of diverse large membrane-bound cargoes causes an acute, albeit transient, radial expansion of the axonal diameter, which is immediately restored by constricting forces. We demonstrate that non-muscle myosin II (NM-II) forms ~200 nm periodic structures, which associate with axonal F-actin rings. Inhibition of NM-II activity with blebbistatin significantly increases axon diameter without affecting the periodicity of either the F-actin rings or NM-II. This sustained radial expansion significantly affects the trafficking speed, directionality, and reduces the overall efficiency of long-range retrograde axonal cargoes, eventually leading to focal axon swelling and cargo accumulation, which are hallmarks of axonal degeneration.

Introduction

Neurons are polarized cells that contain many nerve terminal boutons separated from the cell body by a long and thin axon. Within the axon, an active bidirectional cargo transport system mediates the trafficking of proteins, lipids, membrane-bound vesicles and organelles (cargoes) that undergo retrograde or anterograde transport. Tightly regulated axonal transport is pivotal for neuronal development, communication and survival[1, 2]. Despite the heavy trafficking, quantitative electron microscopy studies have found that thin axons (inner diameter < 1 μm) are the most abundant type in the mammalian central nervous system (CNS)[3, 4]. For instance, the long-range connective axons found in the human corpus callosum have an average diameter that ranges

between 0.64 μm and 0.74 μm^3. In contrast, the size of axonal cargoes is highly variable, encompassing autophagosomes (0.5-1.5 μm)[5], mitochondria (0.75-3 μm)[6] and endosomes (50 nm-1 μm)[7]. Thus, the range of cargo sizes is comparable to, or surprisingly even larger than some of the CNS axons themselves. This advocates for the existence of radial contractility in the axons, which would allow the transient expansion of axon calibre and facilitate the passage of large cargoes. Indeed, the expansion of axonal diameter surrounding large cargoes, *i.e.* autophagosomes[8] or mitochondria[9], has been observed by super-resolution microscopy and 2D-electron microscopy (EM) in both normal and degenerating axons[10, 11]. Considering the spatial limitation exerted by the rigid axon membrane[12], the trafficking of large cargoes is likely to be affected. In fact, a simulation study based on axon structure and intra-axonal microfluidic dynamics predicted that cargo trafficking was impeded by the friction from the axonal walls in small-calibre axons[13]. In line with this prediction, a correlation between axon diameter and axon trafficking was recently reported in *Drosophila*[14, 15] and rodent neurons[16, 17]. However, direct evidence showing whether and how axonal radial contractility affects cargo trafficking is still lacking.

We hypothesized that the underlying structural basis for axonal radial contractility is the subcortical actomyosin network, which is organized into specialized structures called membrane-associated periodic cytoskeletal structures (MPS), as revealed with super-resolution microscopy along the shafts of mature axons[18]. F-actin, together with adducin and spectrin, forms a subcortical lattice with a ~190 nm periodic interval covering the majority of the axon length[18, 19]. The disrupting of axonal F-actin leads to loss of MPS[20, 21], whereas the depletion of adducin causes progressive dilation of the axon diameter and axon loss, with slightly impaired axonal trafficking[16]. The fact that

adducin knock-out axons are still capable of decreasing the diameter of actin rings over time suggests the existence of additional actin regulatory machineries that maintain this constriction. Indeed, the dynamic contractility of the subcortical actomyosin network depends on non-muscle myosin-II (NM-II)[22], which generates the subcellular forces required to restore the shape of the cell following acute stretching[23]. In line with this function, the activated regulatory light chain (pMLC) of NM-II has recently been shown to exist in periodic patterns in close association with the MPS in the axon initiation segment (AIS) of mammalian CNS neurons[24], with actomyosin-dependent contractility being implicated in maintaining axon diameter by coupling the radial and axial axonal contractility in *Drosophila*[14]. Understanding how the dynamic cytoskeletal architecture coordinates the radial axonal contractility and cargo trafficking is therefore warranted.

In this study, we used super-resolution live-imaging approaches to examine the correlation between the speed of axonal cargoes undergoing long-range transport and their size. We found that the speed inversely correlates with the cargo size, and that the axon undergoes dynamic local deformation during the passage of large cargoes, which induces transient enlargement immediately followed by constriction of the axon diameter. We further demonstrated, using super-resolution structured illumination microscopy (SR-SIM) as well as simulated emission depletion (STED) microscopy, that this transient change in axon diameter is mediated by NM-II, which forms an approximately 200 nm periodical structure perpendicular to the longitudinal axis of axons. Our results suggest that CNS axons are under constitutive radial constriction, which limits their diameter. Accordingly, short-term inhibition of axonal NM-II activity with blebbistatin, a specific membrane-permeable inhibitor that stabilizes myosin-II in an actin-detached state[25], does not affect the periodicity of either F-actin or NM-II itself,

but rather effectively decreases their colocalization and expands the diameter of the axon. As a result of augmented axon diameter, short-term blebbistatin incubation affects the transport speed of large cargoes by increasing both the speed of fast-moving cargoes and the back-and-forth movements of stalled ones. This leads to an increase in cargo mobility at the expense of overall trafficking efficacy. Prolonged NM-II inactivation by either blebbistatin treatment or transfection of a myosin-II regulatory light chain (MRLC) loss-of-function mutant eventually leads to the formation of focal axon swellings (FAS) and the accumulation of retrograde cargoes along the axons. In conclusion, our study reveals the critical role of axonal NM-II which, by associating with subcortical MPS in the axon shaft, provides subcellular radial constriction that minimizes the axonal swelling and undirected cargo movements. It therefore ensures the structural stability as well as the cargo-trafficking efficiency along the small-calibre axons.

Results

The speed of retrograde axonal cargoes is inversely correlated with their size.

Large axonal cargoes such as endosomes, lysosomes, autophagosomes and mitochondria tend to accumulate in FAS under pathological conditions[26], suggesting that the size of cargoes might alter the axonal trafficking efficacy. To determine the relationship between the size of cargoes and their transport speed, we analyzed the speeds of various-sized retrograde lysosomal and endosomal vesicles. These cargoes were generated and fluorescent-labelled with the lysosomal marker Lysotracker or the endosomal marker Cholera toxin subunit B (CTB) at the nerve terminals, and underwent retrograde trafficking along the axon bundles of live hippocampal neurons cultured in microfluidic devices (Fig. 1a, b). Hydrostatic pressure was used to restrict

the labelling reagents to the terminal chamber during the 5 min pulse-labelling (Fig. 1c). This was followed by a thorough wash in culture medium to remove the excess fluorescent probe and confocal time-lapse imaging and automatic tracing of the fluorescently tagged cargoes as previously described[8, 27, 28]. To investigate different stages of axonal trafficking, live-imaging was performed in two distinct axonal regions: (1) the axon shafts adjacent to the soma chamber (Fig. 1d, left) and (2) within the terminal chamber (Fig. 1d, right). Lysotracker-labelled vesicles detected in the nerve terminal chamber exhibited very confined movements (sFig. 1a and sMov. 1). We further quantified the average speed of these tracks, which were sorted into two different groups according to their diameter (sFig. 1a, bottom panels). We observed that vesicles with a large diameter ('large', diameter > 0.5 μm) moved significantly slower (0.115 ± 0.039 μm/s) than those with a smaller diameter ('small', diameter ≤ 0.5 μm; 0.159 ± 0.006 μm/s), as shown in sFig. 1b. This suggests that transport of large axonal cargoes in axons surrounding nerve terminals could be impeded during their transit. To specifically investigate the correlation between the size of axonal cargoes and their active transport speed, we further examined the trafficking speed of long-range CTB-positive retrograde carriers in the soma-proximal axon channels (Fig. 1e-g). Consistent with our previous study[29], these long-range carriers exhibited a much faster trafficking speed (0.974-1.659 μm/s) than the carriers at nerve terminals (0.115-0.159 μm/s; Fig. 1g; sFig. 1b). Similar to the lysosomes in the nerve terminals, the trafficking speed of these CTB-positive carriers also inversely correlated with their diameter, with small-diameter cargoes moving faster (1.657 ± 0.06 μm/s) than large-diameter ones (0.974 ± 0.05 μm/s; Fig. 1g; sMov. 2). We then examined the correlation between cargo size and speed by plotting the apparent diameter of either lysosomal carriers or CTB-positive carriers against their speed. This revealed a negative correlation, with a Pearson's

coefficient of -0.303 ± 0.095 and -0.273 ± 0.036 between cargo diameter and trafficking speed in the terminal ("Lysotracker", Fig. 1h) and proximal ("CTB", Fig. 1h) axons, respectively, indicating that the speed of the trafficked cargoes declines as the cargo size increases.

Transit of large cargoes causes a significant radial expansion of the axon.

Each organelle undergoing retrograde axonal transport is driven by multiple dyneins, which are stochastically activated and collectively drive cargo transport through the axonal cytosol[30-32]. Given the low viscosity of axonal cytosol, the force generated by cooperative dyneins is sufficient to ensure their retrograde trafficking through the axon[32]. Thus, the reduced speed of the larger cargoes we observed is unlikely due to insufficient driving force or a higher viscous load due to the larger size. Considering the recent evidence suggesting the role of axon diameter in axon cargo trafficking[14-16], we hypothesized that the size-dependent friction on the axonal cargoes comes from the constrictive force exerted by the axonal plasma membrane, which is more likely to impede the transport of larger retrograde cargoes.

To test this hypothesis, we examined the diameter of axons in the presence or absence of cargoes at the ultrastructural level. In order to eliminate confounding factors related to the analysis of dendrites, experiments were only performed on axonal bundles formed within the channels of microfluidic devices[8, 27, 28], as shown in Fig. 2a. We first used EM to visualize the morphology of both axon shafts and their internal cargoes. As demonstrated in Fig. 2b-c, on the parallel axonal bundles, the diameters of axons were indeed significantly increased around large cargoes, such as large endosomes (Fig. 2c, i, arrow), mitochondria (Fig. 2c, ii and iii, white arrowheads) and autophagosomes (Fig. 2c, iii and iv, black arrowheads). When we measured the diameter of the axonal

segment with (red) and without cargo (blue) in the same axon, we found that those with cargoes had a significantly larger diameter (347 ± 15.6 nm) than those without cargoes (259 ± 9.4 nm; Fig. 2d) with paired comparison. We also observed that, as the size of the cargoes increased, the extent of axon expansion also increased proportionally (Fig. 2e, f), suggesting that the stretch of the axon membrane is indeed caused by the transiting cargo.

We next investigated the effect of transiting cargoes on the diameter of axons in live hippocampal neurons. To effectively label the subcortical actomyosin network in axons, we used Lifeact-GFP, a peptide that binds to both actin filaments (F-actin) and cytosolic actin monomers[33]. Similar to a previous study[34], with the resolution of SIM, we detected Lifeact-GFP distribution in both the filamentous and cytosolic fractions in axons of live hippocampal neurons (Fig. 3a), with the plasma membrane labelled by CTB-Alexa555. Interestingly, the improved 3D-SIM resolution allowed us to observe various-sized intra-axonal fluorescence voids ("black-holes") that likely represent axoplasmic organelles (Fig. 3b), which are known to exclude actin from their lumens[35]. Similar to the cargo-induced axon dilation observed with EM, the axon diameter was also significantly expanded in axon segments with black-holes (Fig. 3c). We then characterized the nature of these black-holes by comparing their localization with that of various organelle markers resolved by 3D-SIM, and found substantial overlap with autophagosomes (LC3-mRFP, Fig. 3d), late endosomes (Rab7-mRFP, Fig. 3e) and mitochondria (Mito-TagRFP, Fig. 3f). This suggests that these black-holes were indeed created by large organelles, which caused significant local dilation of the axon (Fig. 3g). To further investigate whether these black-holes were cargoes that associate with the transport machinery, we determined their colocalization with markers of retrograde

carriers, such as terminal-derived CTB[27] and the neuron-specific dynein intermediate chain 1B (DIC^{1B})[36]. The black-holes partially overlapped with CTB- and DIC^{1B}-positive axonal structures (Fig. 3h, i), indicating that a substantial portion of them were indeed caused by retrograde trafficking organelles in live axons.

Next, we investigated whether the transit of cargoes correlated with the local axon dilation in live axons. Using time-lapse SIM and unbiased Gaussian fitting (Fig. 4a), we assessed the fluctuations in axon diameter and clearly detected radial diameter expansion through the transient separation of the two lateral axonal membranes, which caused an increase in the distance between the centre of the Gaussians (Fig. 4b; sMov. 3). This effect was transient and the initial diameter was restored after the passage of the organelles (black-holes), as shown in Fig. 4c. In addition, the association between diameter expansion and the passage of lysotracker- and CTB-positive carriers was also observed by phase-contrast confocal microscopy (Fig. 4d-e). Taken together, our results demonstrate that radial dilation of the axon diameter is caused by the passage of cargoes in the axons of live hippocampal neurons.

NM-II forms periodic structures that associate with F-actin MPS and controls the radial contractility of axon.

The contractility and plasma membrane tension of cells is controlled by NM-II. To investigate whether NM-II is involved in the cargo-associated radial dilation of axons, we treated Lifeact-GFP-expressing neurons with blebbistatin, and examined the cargo-associated diameter fluctuations of their axons. We observed that blebbistatin treatment (10 µM, 60 min) caused a significant relaxation of the axon shaft by increasing axon diameter with (ϕ_{+cargo}) and without (ϕ_{-cargo}) cargoes (Fig. 5a, b). We then explored the

diameter fluctuations by comparing the average ratio of axon diameter containing cargoes to that without cargoes, and used this ratio ($\phi_{+cargo}/\phi_{-cargo}$) as an index of the cargo-associated diameter fluctuations. Blebbistatin treatment significantly decreased this index, resulting in more uniformly dilated axons (Fig. 5c). These results suggest that radial contractility of the axon shaft is dependent on the NM-II activity of the actomyosin network.

To further explore the molecular basis of the axonal radial contractility, we sought to resolve the actomyosin structure along the axon shafts. As F-actin and its associated proteins are known to form MPS in axons[18, 19, 21], we first aimed to characterize the actin MPS along the axon shaft using SIM, which had previously been used to accurately visualize axon MPS[37]. In cultured hippocampal neurons, phalloidin staining of F-actin allowed the observation of MPS formed along the axon shaft with a conserved longitudinal spacing of ~190 nm (Fig. 5d; sFig. 2a), as quantified using the frequency distribution of spacing between adjacent actin peaks detected using phalloidin-647 (191.8 ± 2.3 nm; Fig. 5e-f; sFig. 2b) or Lifeact-GFP (sFig. 2c-g), and confirmed by auto-correlation analysis (184.6 ± 4.1 nm; Fig. 5g). Obtained values were similar to those previously reported in rat hippocampal axons[18, 21]. As NM-II is involved in the regulation of axonal diameter[14] and associated with the MPS in axons[24], we also examined whether blocking NM-II activity affected the spacing of actin MPS. 60 min of blebbistatin treatment had no effect on this spacing (Fig. 5e, f). However, this short-term treatment significantly increased the radial diameters of the actin rings in treated axons (Fig. 5d, h), causing a more uniformly dilated actin MPS, as reflected by the decreased ring diameter fluctuation (Fig. 5i). These results are consistent with the effect of blebbistatin on axonal diameter expansion in live axons. The significant dilation of

actin MPS caused by detaching NM-II suggests that the interaction between NM-II and actin MPS underlies the radial contractility of axons.

To examine this hypothesis and assess the relationship between the distribution of endogenous NM-II and actin MPS along the axon shaft, we used dual-colour 3D-SIM . We co-labeled the axons of DIV14 rat hippocampal neuron with phalloidin and an antibody that recognizes the C-terminus central domain of NM-IIB (αNM-II(ct)), the dominant form of NM-II in axons[24], and we observed that NM-II exhibited a periodic distribution (Fig. 6a, b), with an average spacing of 197.5 ± 3.1 nm (Fig. 6c, d), which is similar to the periodicity determined by the autocorrelation method (187.4 ±9.8 nm, Fig. 6e). To further examine the orientation and periodicity of the NM-II filaments along the axon, we used another NM-IIB antibody that recognizes its N-terminal head domain (αNM-II(nt)) and which was previously used to detect a bipolar structure of NM-II filaments with super-resolution microscopy[38, 39]. Using super-resolution stimulated emission depletion (STED) microscopy (sFig. 3a), we found that the αNM-IIB(nt) stained for a bipolar structure that had a periodic spacing of 206.4 ± 2.6 nm along the axons (sFig. 3c). These values were consistent with that of phosphorylated-MLC spacing, as reported recently[24]. Interestingly, these bipolar NM-II structures presented a perpendicular orientation to the axon axis in both mono-colored αNM-IIB(nt) stained axons detected by 3D-STED (sFig. 3b) and the dual-colored αNM-IIB(nt) and αNM-IIB(ct) co-stained axons detected by 3D-SIM (sFig. 3d, e).

We also examined the correlation between the actin and NM-II MPS distribution, and noted that they exhibited both overlapping (arrows, Fig. 6b; sFig. 4a, b) and alternating (arrowheads, Fig. 6b; sFig. 4a, b) distribution patterns, which were reflected by the high

cross-correlation coefficient of 0.684 ± 0.091 (Fig. 6f, at 0 nm shift). However, we failed to detect an obvious cross-periodicity between actin and NM-II (Fig. 6f), which was probably due to the fact that the periodicity between these two patterns is beyond the resolution limit of SIM (~100 nm). We next investigated whether the localization pattern of NM-II was affected by the inhibition of its activity, and found that short-term blebbistatin treatment did not significantly change the NM-II spacing (Fig. 6c-e), but significantly decreased the degree of cross-correlation between NM-II and actin MPS (0. 414 ± 0.073 (0 nm); Fig. 6f). Indeed, it was apparent that NM-II and actin MPS distributed more discretely from each other in the axons of blebbistatin-treated neurons (Fig. 6a, b, bottom panels). This reduction in NM-II and actin correlation was further supported by the reduced colocalization between NM-II and actin voxels following blebbistatin treatment, as resolved from the 3D-SIM images (sFig. 4b-d).

To confirm that the NM-II indeed correlated with actin MPS in the subcortical network, which is associated with the axonal plasma membrane, we adopted the method of Triton X-100 extraction before fixation to specifically remove the subcortical actin MPS components as previously reported[20]. Following this extraction, we observed a significant reduction in actin MPS (sFig. 4e, f), confirming the disruption of the membrane-associated actin MPS. Together with this reduction, we detected a dramatic reduction in NM-II positive puncta (sFig. 4e, g). This concomitant decrease in both actin MPS and NM-II (sFig. 4h) further supports the notion that NM-II correlates with actin MPS in the membrane-associated subcortical network. Together, these results indicate that NM-II controls the contraction of the subcortical actin MPS, which underlies the radial contractility of axons.

Short-term inhibition of NM-II activity causes sustained axon dilation and interferes with the long-range retrograde trafficking of large cargoes.

To test whether axon radial contractility has a functional role in cargo transport, we examined the effect of blebbistatin on retrograde axonal trafficking in neurons grown in a 6-well microfluidic device (sFig. 5a), where we could restrict the action of blebbistatin to the axon segments by adding it through the middle chamber (sFig. 5b). Widespread dilation of the axons diameter along their longitudinal direction was observed following 90 min of blebbistatin incubation (sFig. 5c-e). To test the integrity of these treated axons, we further examined the axonal microtubule structure by dual-color SIM using a β-tubulin III antibody and phalloidin (sFig. 5f). We found that neither the microtubule bundle intensity (sFig. 5g) nor width (sFig. 5h) were affected by 60 min blebbistatin treatment. This blebbistatin treatment also failed to affect the mitochondrial anchoring, as the movement of the immobile mitochondrial fraction was not affected (sFig. 5i, j), whereas the mobile fractions with the higher average speeds were significantly increased by the blebbistatin movement (sFig. 5i, j), suggesting that the NM-II-dependent axonal contractility is likely to affect the cargo transport.

To further assess the effects of axonal contractility on cargo trafficking, we examined the impact of disrupting NM-II activity on retrograde trafficking in short-term blebbistatin-treated axons. The average speed of CTB-positive carriers before (pre) and after (+BLB) blebbistatin treatment for 60 min (Fig. 7a) were compared. As demonstrated earlier (Fig. 1g), small carriers moved faster than large ones in the absence of blebbistatin (Fig. 7b), whereas blebbistatin treatment specifically increased the trafficking speed of large CTB-positive carriers, but not that of small ones (Fig. 7b and sMov. 4). Similarly, an increase of the average speed was observed for large

317 Lysotracker-positive carriers, but not for small ones (Fig. 7c, sMov. 5). These results
318 indicate that the short-term relaxation of the axonal actomyosin-II network has an initial
319 positive impact on the trafficking of large cargoes, suggesting that axon radial
320 contractility exerts a local brake on their transport.
321
322 Given that the large CTB-positive carrier population showed the most significant
323 increase in speed upon blebbistatin treatment (Fig. 7b), we chose this type of carriers
324 for more detailed motion analyses, in order to further dissect the impact of radial
325 contractility on axonal transport. By tracking the transport of individual CTB-carriers
326 within the microfluidic channels (Fig. 7a), we noted that their trajectories were
327 predominately composed of two mobility states: (i) a fast-moving state and (ii) a stalled
328 state, as indicated by the sloped and the vertical lines, respectively, in the displacement-
329 time plot (Fig. 7d). Following 60 min blebbistatin treatment, the speed of the fast-
330 moving state was significantly increased, as indicated by the flatter slopes (Fig. 7d),
331 whereas in the stalled state we observed pronounced back-and-forth motion (Fig. 7d,
332 asterisks and sMov. 4), which has been previously described as low-efficiency
333 trafficking pattern for long-range cargo transport[40]. We noticed an increase in the ratio
334 of the fast-moving CTB-carriers (sFig. 5k) and a decrease in that of the slow-moving
335 ones (sFig. 5k). To further quantify these back-and-forth movements, we compared the
336 ratio of direction swap (*Sr*) in these tracks by measuring the ratio of the time cargoes
337 spent travelling in the reverse direction (t_{rev}) in relation to the total time travelled (t_{total}),
338 as shown in equate (1), with k being the number of trajectories.

339 $$Sr = \frac{\sum_{k=0}^{n} {t_{rev}}^k}{\sum_{k=0}^{n} {t_{total}}^k} \quad (1)$$

This analysis revealed that blebbistatin treatment significantly increased the amount of time cargoes underwent reverse motion, thereby increasing the ratio of direction swap in cargoes moving along the axon (Fig. 7e). Accordingly, we found that blebbistatin treatment decreased the number of CTB-positive carriers that traversed the imaging window within a given time (Fig. 7f), suggesting that the overall retrograde trafficking efficiency was reduced. These results support the positive role of axonal radial contractility in maintaining near-unidirectional retrograde trafficking, thereby ensuring the overall efficiency of long-range retrograde transport.

We next investigated how the radial contractility impacted the mobility of the fast-moving and stalled carriers, respectively, by analyzing the dynamics of the CTB-positive carrier movements. To objectively and quantitatively analyze the effect of the contractility on the two motion states, we employed a two-state hidden Markov model (HMM) to annotate these CTB trajectories into stalled (D) and transport (DV) states (Fig. 7g), as previously described[28]. The separating efficacy of this model was demonstrated by the fact that the step size of the stalled (0.1168 ± 0.45 μm) and transport states (0.4352 ± 1.53 μm) were distinct from each other. We then examined the effect of blebbistatin treatment, and found that it significantly increased the step size of large CTB-positive carriers in the DV state (Fig. 7h, pink spots), which is in good agreement with our earlier observations (Fig. 7b and sMov. 4). For the D state in pretreated axons, CTB-positive carriers exhibited a much smaller step size (Fig. 7h), meaning that the mobility of these stalled carriers was constrained. However, this limited step size was significantly increased following 60 min blebbistatin treatment (Fig. 7h, blue spots). Consistent with the increased back-and-forth movements (Fig. 7d, e), this result suggests that the mobility of the stalled carriers is increased following

365 disruption of NM-II activity. Taken together, our findings indicate that the axonal
366 actomyosin network maintains radial constriction, which not only impedes the speed of
367 the fast-moving state but also suppresses the low-efficiency back-and-forth movement
368 during the stall state of these long-range carriers. The overall impact of this contractility
369 on long-range trafficking is therefore positive, which facilitates the uni-directionality
370 and the overall efficiency of long-range retrograde carriers.
371
372 ***Prolonged inactivation of actomyosin-II causes focal axon swelling accompanied***
373 ***with stalled cargo accumulation.***
374 In addition to 60 min blebbistatin treatment, we also examined the impact of longer
375 exposure to blebbistatin on both axon structure and trafficking. We discovered that
376 prolonged blebbistatin treatment (60 - 120 min) increased the percentage of axons with
377 focal swellings (Fig. 8a, b), which was represented by the gradual formation of FAS
378 (Fig. 8a), with these FAS becoming prevalent (59.85 ± 5.159 %) following long-term
379 blebbistatin treatment (10 μM, 120 min, Fig. 8b). As FAS is a hallmark of irreversible
380 axonal damage[11], these results suggested that disrupting radial contractility could
381 directly lead to FAS and ensuing axonal degeneration.
382
383 To fully assess the effects of radial axon contractility on retrograde cargo trafficking,
384 we further resolved the impact of long-term NM-II inhibition on the long-range
385 trafficking of retrograde endosomal CTB-positive carriers (Fig. 8c). We found that both
386 the trafficking speed (Fig. 8d) and transverse frequency (Fig. 8e) of these carriers were
387 significantly reduced after 120 min blebbistatin treatment. To assess whether the axonal
388 radial contractility affects trafficking efficiency of other retrograde cargoes, we also
389 compared the trafficking efficacy of autophagosome (LC3-mRFP labelled), which

undergoes long-range retrograde trafficking[8, 41], in axons in the presence or absence of blebbistatin (120 min treatment). We found that similar to CTB-positive carriers, the trafficking speed of these LC3-mRFP-positive carriers was also significantly reduced (Fig. 8f, g). Importantly, we also observed the gradual accumulation of the stalled LC3-carriers at FAS (Fig. 8f, h). In addition to pharmacological inactivation of NM-II, we also transfected the myosin-II regulatory light chain with the S19AT18A mutations, (MRLC^{mut}-GFP), which abolishes the ability of NM-II to bind to and slide along the F-actin[42]. We found that 48 hours after MRLC^{mut}-GFP transfection, the structural integrity of transfected axons was significantly disrupted as reflected by the significantly increased diameter fluctuations (Fig. 8i, j) and FAS formation (Fig. 8k) compared to those transfected with wild-type controls (MRLC^{wt}-GFP). These results suggest that the long-term inactivation of actomyosin-II not only impairs axonal trafficking but also causes irreversible structural damage to the axon, which may eventually lead to its degeneration.

Discussion

Many factors affect long-range axonal cargo trafficking, including the number and type of attached molecular motors[43, 44], the polarity of the microtubule tracks[45], and friction from other organelles[46]. With the development of live-imaging microscopy, most of these factors have been extensively studied in cell-free *in vitro* systems[44], and within the axons of cultured neurons[32, 47] and live animals[48]. However, the impact of the narrow and rigid axonal plasma membrane on the transiting cargoes remains largely elusive. In this study, we have demonstrated that the transport of large membrane-bound cargoes causes an acute, albeit transient, radial stretching of the axonal plasma membrane, which is immediately restored by constitutive constricting forces generated by the membrane-associated periodic actomyosin-II network. We have also identified NM-II as a critical regulator of this radial contractility, which controls not only the speed but also the directionality of long-range cargo trafficking along the axon. Inactivation of this contractility machinery eventually leads to stalled cargo trafficking and FAS, which are early signs of axon degeneration. Our study therefore reveals novel functions of the actomyosin-II network in facilitating the efficacy of long-range axonal trafficking and maintaining the structural stability of CNS axons.

Radial contractility facilitates the overall efficiency of long-range retrograde axonal trafficking.

An efficient long-range retrograde cargo transport machinery is critical for the survival and function of neurons[1, 2, 48]. Retrograde trafficking is thrusted by cytoplasmic dynein[49], which drives the near-unidirectional retrograde transport of nerve terminal-derived signalling endosomes and autophagosomes to the cell body[8, 32]. Detailed analysis of the

429 movement of these carriers has revealed that they are mainly composed of fast-moving
430 retrograde-directed and stalled carriers, with less than 3% being reverse-directed
431 (anterograde) carriers[8, 27]. A similar near uni-directional motion pattern is shared by
432 retrograde endosomes carrying nerve growth factor (NGF)[32] and tetanus toxins[50]. The
433 retrograde directionality of the fast-moving cargoes is driven by the progressive minus-
434 end-directed dynein steps, the directionality of which is dependent on the opposing
435 forces they received[49]. Actomyosin controls radial contractility, which poses a steric
436 hindrance to the passaging cargoes[46] and therefore could potentially affects the
437 opposing force to their driven dyneins. However, the effect of the axonal actomyosin
438 network on the dynein-driven trafficking is poorly understood. Early studies provided
439 evidence that disrupting F-actin in axons does not interfere with organelle transport,
440 which continues unabated or at an even faster rate[51], suggesting that the axonal F-actin
441 network acts as a physical impediment to cargo transport. In line with this, we found
442 that short-term blebbistatin treatment released subcellular tension, causing an
443 expansion of the axon diameter and specifically increasing the transport speed of large
444 cargoes. Our results therefore confirm that the fast-moving state of large cargoes is
445 subjected to a constant impediment from radial axonal constriction. On the other hand,
446 the stalling of retrograde carriers is likely to be caused by either a balanced tug-of-war
447 between kinesin and dynein[52], or the transient detachment of dynein-driven carriers
448 from the microtubule tracks[40, 49]. Our data using HMM-Bayesian partition show an
449 increased mobility of stalled carriers after blebbistatin treatment, which suggests that
450 axonal radial constriction might affect the microtubule attachment/tethering of these
451 stalled carriers within the axon. This could be due to the tension-dependent tethering of
452 dynein to the microtubule tracks[53]. However, further study on the coordination between
453 cargo trafficking and local axon radial tension, using higher temporal resolution live-

imaging techniques, is needed to establish the precise relationship between axonal radial constriction and the motion of various-sized retrograde carriers.

The actomyosin-II network is the structural basis for the contractility of axon shafts. The diameter of the long and thin axon has long been believed to be uniform for the same type of neurons. However, with the development of 3D EM reconstruction, diameter fluctuations have been detected along the length of axons in optical nerves[10]. Similarly, in live rat brains, axonal diameter fluctuations were revealed with super-resolution microscopy after the conduction of action potentials[54]. Consistent with these *in vivo* studies, we have used EM, SR-SIM and bright-field confocal microscopy to reveal that axons undergo dynamic diameter fluctuations. With time-lapse SR-SIM and confocal microscopy, we further correlated the dynamic radial expansion of the axonal diameter with the passage of large cargoes. These deformations are highly correlated with the transit of various types of large cargoes and are therefore most likely caused by this. These transient deformations also suggest the existence of a mechanical tension derived from the axonal plasma membrane. Atomic force microscopy studies have identified the axon as the most rigid neuronal segment, which is under constitutive tension[12] from the ordered periodic longitudinal MPS composed of actin, spectrin, adducin and associated proteins[18]. Disruption of actin and spectrin abolished the actin MPS, whereas adducin depletion did not affect its spacing but still caused dilation and degeneration of axons[16]. However, the radial contractility of adducin knockout axons remained unaltered, suggesting the existence of an alternative mechanism for the contractility along the axon shafts.

In mammalian cells, radial contractility of subcortical actin[55] or actin rings[35] is regulated by mechanosensory NM-II, which is the major cytoskeletal complex in neurons with the ability to convert ATP into mechanical force. Recently, the activated form of NM-II light chain (pMLC) was shown to distribute in a similar periodicity and largely overlap with the actin MPS at the AIS[24]. Moreover, depolarization rapidly decreased NM-II activity, further suggesting that this constricting structure is highly dynamic[24, 56]. Consistent with these previous studies, we reveal a periodic pattern of NM-II of ~200 nm by dual labelling with phalloidin-647 and an NM-IIB C-terminus antibody. In addition, cross-correlation analysis of these two MPS demonstrates a substantial colocalization, which is significantly reduced by blebbistatin-induced NM-II detachment. Further, our results demonstrate that NM-II periodicity goes far beyond the AIS, and confirm the existence of periodic actomyosin rings, which provide the structural basis for axonal radial contractility. Higher resolution three-colour microscopic techniques are needed to further resolve the precise conformational changes that occur at the level of the actomyosin-II MPS as large cargoes pass through.

Over-expansion of axonal segments, such as FAS, has been noted in several neurodegenerative diseases, with the accumulation of organelles and cargoes at the axonal swellings - the presence of FAS is generally regarded as an early sign of axonal degeneration[11]. Similar to FAS, diameter dilation, cargo accumulation and degeneration were also observed in axons of adducin knock out mice[16], as well as in axons following prolonged blebbistatin treatment (>120 min) or transfection with the inactive MRLC mutant in this study, suggesting that the actomyosin-II-dependent radial contractility is critical to maintain the structural stability of the axon. Additional studies will be

502 required to directly characterize the contractility changes in FAS and to examine
503 whether enhancing radial contractility could have any rescuing effect.
504
505 In summary, we have uncovered an inverse correlation between axonal cargo size and
506 trafficking speed, and demonstrated that axons undergo transient deformation caused
507 by the cargo transition in hippocampal axon bundles. We have further identified the
508 periodic structure of actomyosin-II along the axon shaft as the structural basis of axonal
509 radial contractility. We have also characterized its role in facilitating long-range cargo
510 trafficking by restricting inefficient back-and-forth cargo movement during the stall
511 state. Our data identify a novel role for the axonal actomyosin-II network in long-range
512 cargo trafficking, and highlight the importance of axonal membrane tension in ensuring
513 the efficiency of this trafficking.
514

Online Methods

Antibodies, molecular reagents and DNA constructs

Alexa-555- and Alexa-647-conjugated recombinant CTB were obtained from ThermoFisher Scientific (#c-34776, #c-34777). Mouse anti-synaptobrevin-2 (VAMP2) antibody was obtained from Synaptic Systems (#104 211) and the rabbit anti-NM-IIB(ct) polyclonal antibodies were from Sigma-Aldrich (#M7939), mouse anti-NM-IIB(nt) monoclonal from Santa Cruz (sc-376954). Alexa-647-phalloidin was purchased from Invitrogen (#A22287), while the mouse anti- β-tubulin III was from Covance (#MMS-435P). Alexa Fluor secondary antibodies were purchased from Life Technologies. The DNA construct encoding Lifeact-GFP was provided by Roland Wedlich Soldner (MPI Biochemistry, Martinsried), pTagRFP-mito was purchased from Evrogen (#FP147), pmRFP-LC3 was a gift from Tamotsu Yoshimori (Addgene plasmid # 21075). Lysotracker Deep Red came from ThermoFisher (#L12492). The remaining reagents were obtained from Electron Microscopy Sciences or Sigma Aldrich unless otherwise specified.

Neuronal cultures

Hippocampal neurons were cultured from embryonic day 18 (E18) embryos from Sprague Dawley rats. All experiments were approved by The University of Queensland Animal Ethics Committee. Hippocampal neurons were prepared as described previously[8] and were plated on either glass coverslips (for confocal microscopy), plastic dishes (for EM) or in microfluidic chambers (Xona, #RD450) according to the manufacturer's protocol[57]. For the pretreated groups, live-imaging of approximate 5 (30×12 μm) regions of interest (ROIs) was performed 2 h after the CTB labelling. For blebbistatin treatment, conditioned culture medium containing blebbistatin (10 μM)

was only added to the middle and/or terminal chambers of the 6-well or 4-well microfluidic chambers (Xona, #TCND500; #RD450) to exclude its effect on the soma. For the short-term blebbistatin treatment, microfluidic devices were immediately returned to the 37ºC imaging chamber for live imaging, and approximately 5 ROIs were imaged within a total duration of 60 min. For long-term blebbistatin treatment, microfluidic devices were returned to a 37ºC CO_2 incubator for an additional 2h before continuing the live imaging.

Confocal microscopy

Stimulation and labelling were carried out on rat hippocampal neurons cultured in microfluidic chambers between day *in vitro* 14 (DIV14). Briefly, the culture medium was removed from all chambers and the neurons were incubated for 5 min at 37˚C in labelling buffer (15 mM HEPES, 95 mM NaCl, 56 mM KCl, 2.2mM $CaCl_2$, 0.5mM $MgCl_2$, 5.6mM D-glucose, 0.5 mM ascorbic acid, 0.1% bovine serum albumin (BSA), pH 7.4), with 50 ng/ml CTB-Af555 or CTB-Af647 added to the nerve terminal chambers only. For Lysotracker labelling, the incubation time was 30 min. Neurons were then washed 3 times with warm neurobasal medium and returned to the original conditioned growth medium for 2 h prior to imaging. Images were acquired with a Zeiss LSM710 inverted microscope maintained at 37˚C and 5% CO_2, and movies were analysed for carrier kinetics using the spot function of Imaris software (Imaris7.7-9.2, Bitplane). Kymographs were generated using ImageJ software (NIH) using the plugin Multi-Kymograph for ImageJ. For immunofluorescence microscopy of fixed cells, the microfluidic devices were removed and neurons were subsequently fixed for 2-4 h at 4ºC with phosphate buffered saline (PBS) containing 4% paraformaldehyde and 4% sucrose, followed by immunostaining as previously described[27]. Permeabilization was

565 performed using 0.1% saponin, 0.2% gelatin, and 1% BSA in PBS. Imaging was carried
566 out on a Zeiss LSM710 confocal microscope and analysed with Zen (Zeiss) and ImageJ
567 softwares. All images were compiled using Illustrator CS 5.1 (Adobe).
568
569 ***Imaris tracing of axonal cargoes***
570 Time-lapse movies of CTB-positive or Lysotracker-positive carriers were analysed for
571 carrier kinetics using the spot function of Imaris software (Imaris7.7-9.2, Bitplane). In
572 brief, region growth was enable (threshold 50, diameter from border mode), estimated
573 diameter 0.75 μm, tracing with autogressive motion (Max Distance 2 μm, Max Gap
574 size 0). Resulted trajectories were filtered with duration > 10 s and instant speed > 0.07
575 μm/s. Average speed are calculated as track length divided by track duration. For
576 Lysotracker-positive carriers that bleaches rapidly, only the diameter of the first time
577 point in each trajectory were used as the diameter for size grouping.
578
579 ***Co-labelling of F-actin and NM-II for SR-SIM***
580 Cultured rat hippocampal neurons were fixed at DIV14. For dual-colour imaging of
581 actin and NM-IIB, the fixation protocol was modified from that previously established
582 for maintaining actin ultrastructure[18]. Briefly, the samples were initially fixed in 4%
583 paraformaldehyde dissolved in cytoskeleton buffer (CB, 10 mM MES, 150 mM NaCl,
584 5 mM EGTA, 5 mM glucose and 5 mM $MgCl_2$, pH 6.1) for 30 min at room temperature
585 and then blocked with antibody dilution buffer (2% BSA with 0.1% Triton X-100 in
586 PBS) for 1 h at room temperature, after which the primary antibody (NM-IIB, diluted
587 1 in 500) and phalloidin-Af647 (0.14 μM) in 2% BSA in PBS were applied to the dish
588 and incubated at 4°C overnight. Donkey anti-rabbit secondary antibody (Thermofisher,
589 #A-21206) was diluted at 1/500 and incubated for 1h at room temperature. Samples

were immediately mounted in Vectashield medium (Vector Laboratories, #H-1000) for SIM imaging. For the Triton X-100 extraction experiment, neurons were first treated with the extraction buffer (4% paraformaldehyde, 0.1% (v/v) Triton X-100, 1 μg/ml phalloidin in CB) for 45 s before the fixation and staining steps.

Structured illumination microscopy

Imaging of live or fixed samples was performed using an ELYRA PS1 SR-SIM system (Zeiss) equipped with a 100x objective (α Plan-Apochromat 100×/1.46 oil-immersion DIC M27) and a CMOS camera (PCO Scientific). For live-imaging of the Af555-CTB-labelled neurons, images were obtained with the Fastframe mode (100 ms exposure time, a time serie of 200 frames at 1.44 s intervals, a SIM grating size of 42 μm at 561 nm wavelengths, and using 3 rotations). For fixed and stained samples, images were obtained by acquiring z-stacks of 10-16 slices with a spacing of 0.101 μm, an exposure time of 100 ms, a SIM grating size of 42-51 μm, and using five rotations. 3D structured illumination images were then aligned and processed using the Zen software. For cross-correlation analysis, line profiles were selected based on the standard of the existence of at least 4 consecutive NM-II peaks in a single axon shafts. The intensity profiles of each of the channels were then obtained using the Multichannel plot profile function of BAR collection (DOI10.5281/zenodo.28838) in ImageJ software (NIH). The auto-correlation or cross-correlation rate between the different channels was then examined using the xcorr function of Matlab. The correlation values for each axon segment were averaged and plotted.

Simulated emission depletion (STED) microscopy

614 Cultured rat hippocampal neurons (DIV14-17) cultured in glass bottom dishes were
615 imaged on a Leica SP8 confocal with STED 3X. (DMI8 stand with 775nm, 660nm
616 592nm STED lasers and a white-light tuneable laser for excitation). Images were
617 acquired using the HC plan apochromat 100x 1.4 NA oil immersion objective using
618 Leica LASX software with 3 frame accumulations as multi-slice z-stacks.
619 Deconvolution was performed using up to 40 cycles of iterative deconvolution using
620 Huygens Professional. Images were visualised and maximum intensity projected using
621 FIJI (NIH).
622
623 ***Assessment of actin MPS and NM-II abundance***
624 Periodic cytoskeletal structures (MPS) are defined as the axonal regions with at least
625 4 consecutive actin or NM-II peaks along the longitudinal direction. 5-7 of 5
626 μm × 5 μm ROIs were selected along the axons in each 3D-SIM image (50
627 μm × 50 μm). In each ROI, the length of axon with F-actin MPS was measured with
628 ImageJ by a trained observer blind to the treatment conditions. In the same ROI, the
629 particle number of NM-II staining was also automatically quantified with the
630 Analyse Particle plugin of FIJI. MPS or NM-II abundance were then calculated as
631 the percentage of segments length with an MPS or particle number over the total
632 length of axons in the ROI respectively.
633
634 ***Electron microscopy***
635 Rat hippocampal neurons cultured in microfluidic devices (14-17 DIV) were treated as
636 described for confocal microscopy[27], except that 10 μg/ml CTB-HRP was added to the
637 nerve terminal chambers for the period of stimulation. Cells were returned to growth
638 medium for 4 h prior to fixation. All cells were fixed in 2.5% glutaraldehyde for 24 h.

639 Following fixation, they were processed for 3, 39-diaminobenzidine (DAB)
640 cytochemistry using the standard protocol. Fixed cells were contrasted with 1% osmium
641 tetroxide and 4% uranyl acetate prior to dehydration and embedding in LX-112 resin[58].
642 Sections (~50 nm) were cut using an ultramicrotome (UC64; Leica). To quantify CTB-
643 HRP endocytosis, presynaptic regions were visualized at 60,000x using a transmission
644 electron microscope (model 1011; JEOL) equipped with a Morada cooled CCD camera
645 and the iTEM AnalySIS software. Membrane-bound compartments within the cell
646 soma proximal region of the microfluidic channel were analysed, and the axon diameter
647 measured using ImageJ software.
648
649 ***HMM-Bayes analysis***
650 Hidden Markov model (HMM) method was used to predict the particle hidden states
651 and the state transition probabilities from experimental trajectories. By using Bayesian
652 model selection in the inference process, the simplest mobility model can be selected
653 to describe these trajectories in an objective manner[59]. We analysed the trajectories
654 from each cell of interest using HMM-Bayes software[60]. A maximum of 2 hidden states
655 was set to describe the trajectory movements, diffusion motion (D) and active transport
656 state (DV), which were used to describe the stalled state and the fast-moving state,
657 respectively. In our cases, at least 10 channel ROIs were quantified for the control group
658 and the blebbistatin-treated group, with corresponding trajectory numbers being 126
659 and 190 respectively. The D state with a low apparent diffusion coefficient state
660 representing the immobile unattached movement. The DV state, which could be
661 described by averaged velocity, represents the active transport attached movement. All
662 of the analyses were performed using Matlab (R2016a, MathWorks, Inc.). The average
663 step sizes of different transport states was calculated from all D-DV models.

664

665 ***Statistics***

666 We used GraphPad Prism 7 (GraphPad Inc.) for statistical analyses. Results are reported
667 as mean ± s.e.m. For group comparisons, two-tailed nonparametric *t*-tests or paired *t*-
668 tests were executed. *P* values < 0.05 indicated statistical significance. No statistical
669 methods were used to predetermine sample sizes. Data distribution was assumed to be
670 normal, but this was not formally tested. There was no formal randomization. Data
671 collection and analysis were performed by different operators, who were blind to the
672 conditions of the experiments.

673

References

1. Tojima, T. & Kamiguchi, H. Exocytic and endocytic membrane trafficking in axon development. *Dev Growth Differ* **57**, 291-304 (2015).
2. Barford, K., Deppmann, C. & Winckler, B. The neurotrophin receptor signaling endosome: Where trafficking meets signaling. *Dev Neurobiol* **77**, 405-418 (2017).
3. Liewald, D., Miller, R., Logothetis, N., Wagner, H.J. & Schuz, A. Distribution of axon diameters in cortical white matter: An electron-microscopic study on three human brains and a macaque. *Biol Cybern* **108**, 541-57 (2014).
4. Perge, J.A., Niven, J.E., Mugnaini, E., Balasubramanian, V. & Sterling, P. Why do axons differ in caliber? *J Neurosci* **32**, 626-38 (2012).
5. Mizushima, N., Ohsumi, Y. & Yoshimori, T. Autophagosome formation in mammalian cells. *Cell Struct Funct* **27**, 421-9 (2002).
6. McBride, H.M., Neuspiel, M. & Wasiak, S. Mitochondria: More than just a powerhouse. *Curr Biol* **16**, R551-60 (2006).
7. Altick, A.L., Baryshnikova, L.M., Vu, T.Q. & von Bartheld, C.S. Quantitative analysis of multivesicular bodies (mvbs) in the hypoglossal nerve: Evidence that neurotrophic factors do not use mvbs for retrograde axonal transport. *J Comp Neurol* **514**, 641-57 (2009).
8. Wang, T., *et al.* Control of autophagosome axonal retrograde flux by presynaptic activity unveiled using botulinum neurotoxin type-a. *Journal of Neurochemistry* **134**, 165 (2015).
9. Yin, X., *et al.* Proteolipid protein-deficient myelin promotes axonal mitochondrial dysfunction via altered metabolic coupling. *J Cell Biol* **215**, 531-542 (2016).

10. Giacci, M.K., *et al.* Three dimensional electron microscopy reveals changing axonal and myelin morphology along normal and partially injured optic nerves. *Sci Rep* **8**, 3979 (2018).

11. Maia, P.D., *et al.* Diagnostic tools for evaluating the impact of focal axonal swellings arising in neurodegenerative diseases and/or traumatic brain injury. *J Neurosci Methods* **253**, 233-43 (2015).

12. Zhang, Y., *et al.* Modeling of the axon membrane skeleton structure and implications for its mechanical properties. *PLoS Comput Biol* **13**, e1005407 (2017).

13. Wortman, J.C., *et al.* Axonal transport: How high microtubule density can compensate for boundary effects in small-caliber axons. *Biophys J* **106**, 813-23 (2014).

14. Fan, A., Tofangchi, A., Kandel, M., Popescu, G. & Saif, T. Coupled circumferential and axial tension driven by actin and myosin influences in vivo axon diameter. *Sci Rep* **7**, 14188 (2017).

15. Narayanareddy, B.R., Vartiainen, S., Hariri, N., O'Dowd, D.K. & Gross, S.P. A biophysical analysis of mitochondrial movement: Differences between transport in neuronal cell bodies versus processes. *Traffic* **15**, 762-71 (2014).

16. Leite, S.C., *et al.* The actin-binding protein alpha-adducin is required for maintaining axon diameter. *Cell Rep* **15**, 490-498 (2016).

17. Pesaresi, M., *et al.* Axon diameter and axonal transport: In vivo and in vitro effects of androgens. *Neuroimage* **115**, 191-201 (2015).

18. Xu, K., Zhong, G. & Zhuang, X. Actin, spectrin, and associated proteins form a periodic cytoskeletal structure in axons. *Science* **339**, 452-6 (2013).

19. Han, B., Zhou, R., Xia, C. & Zhuang, X. Structural organization of the actin-spectrin-based membrane skeleton in dendrites and soma of neurons. *Proc Natl Acad Sci U S A* **114**, E6678-E6685 (2017).

20. Zhong, G., *et al.* Developmental mechanism of the periodic membrane skeleton in axons. *Elife* **3** (2014).

21. He, J., *et al.* Prevalent presence of periodic actin-spectrin-based membrane skeleton in a broad range of neuronal cell types and animal species. *Proc Natl Acad Sci U S A* **113**, 6029-34 (2016).

22. Arnold, D.B. & Gallo, G. Structure meets function: Actin filaments and myosin motors in the axon. *J Neurochem* **129**, 213-220 (2014).

23. Papadopulos, A., *et al.* Activity-driven relaxation of the cortical actomyosin ii network synchronizes munc18-1-dependent neurosecretory vesicle docking. *Nat Commun* **6**, 6297 (2015).

24. Berger, S.L., *et al.* Localized myosin ii activity regulates assembly and plasticity of the axon initial segment. *Neuron* **97**, 555-570 e6 (2018).

25. Kovacs, M., Toth, J., Hetenyi, C., Malnasi-Csizmadia, A. & Sellers, J.R. Mechanism of blebbistatin inhibition of myosin ii. *J Biol Chem* **279**, 35557-63 (2004).

26. Tammineni, P., Ye, X., Feng, T., Aikal, D. & Cai, Q. Impaired retrograde transport of axonal autophagosomes contributes to autophagic stress in alzheimer's disease neurons. *Elife* **6** (2017).

27. Wang, T., *et al.* Flux of signalling endosomes undergoing axonal retrograde transport is encoded by presynaptic activity and trkb. *Nat Commun* **7**, 12976 (2016).

747 28. Joensuu, M., *et al.* Visualizing endocytic recycling and trafficking in live
748 neurons by subdiffractional tracking of internalized molecules. *Nat Protoc* **12**,
749 2590-2622 (2017).
750 29. Joensuu, M., *et al.* Subdiffractional tracking of internalized molecules reveals
751 heterogeneous motion states of synaptic vesicles. *J Cell Biol* **215**, 277-292
752 (2016).
753 30. Rai, A.K., Rai, A., Ramaiya, A.J., Jha, R. & Mallik, R. Molecular adaptations
754 allow dynein to generate large collective forces inside cells. *Cell* **152**, 172-82
755 (2013).
756 31. Mallik, R., Petrov, D., Lex, S.A., King, S.J. & Gross, S.P. Building complexity:
757 An in vitro study of cytoplasmic dynein with in vivo implications. *Curr Biol* **15**,
758 2075-85 (2005).
759 32. Chowdary, P.D., Che, D.L., Zhang, K. & Cui, B. Retrograde ngf axonal
760 transport--motor coordination in the unidirectional motility regime. *Biophys J*
761 **108**, 2691-703 (2015).
762 33. Riedl, J., *et al.* Lifeact: A versatile marker to visualize f-actin. *Nat Methods* **5**,
763 605-7 (2008).
764 34. Ganguly, A., *et al.* A dynamic formin-dependent deep f-actin network in axons.
765 *J Cell Biol* **210**, 401-17 (2015).
766 35. Gormal, R.S., Nguyen, T.H., Martin, S., Papadopulos, A. & Meunier, F.A. An
767 acto-myosin ii constricting ring initiates the fission of activity-dependent bulk
768 endosomes in neurosecretory cells. *J Neurosci* **35**, 1380-9 (2015).
769 36. Ha, J., *et al.* A neuron-specific cytoplasmic dynein isoform preferentially
770 transports trkb signaling endosomes. *J Cell Biol* **181**, 1027-39 (2008).

771 37. Qu, Y., Hahn, I., Webb, S.E., Pearce, S.P. & Prokop, A. Periodic actin structures
772 in neuronal axons are required to maintain microtubules. *Mol Biol Cell* **28**, 296-
773 308 (2017).
774 38. Hu, S., *et al.* Long-range self-organization of cytoskeletal myosin ii filament
775 stacks. *Nat Cell Biol* **19**, 133-141 (2017).
776 39. Beach, J.R., *et al.* Nonmuscle myosin ii isoforms coassemble in living cells.
777 *Curr Biol* **24**, 1160-6 (2014).
778 40. Yi, J.Y., *et al.* High-resolution imaging reveals indirect coordination of opposite
779 motors and a role for lis1 in high-load axonal transport. *J Cell Biol* **195**, 193-
780 201 (2011).
781 41. Maday, S., Wallace, K.E. & Holzbaur, E.L. Autophagosomes initiate distally
782 and mature during transport toward the cell soma in primary neurons. *J Cell*
783 *Biol* **196**, 407-17 (2012).
784 42. Beach, J.R., Licate, L.S., Crish, J.F. & Egelhoff, T.T. Analysis of the role of
785 ser1/ser2/thr9 phosphorylation on myosin ii assembly and function in live cells.
786 *BMC Cell Biol* **12**, 52 (2011).
787 43. Hancock, W.O. Bidirectional cargo transport: Moving beyond tug of war. *Nat*
788 *Rev Mol Cell Biol* **15**, 615-28 (2014).
789 44. Vale, R.D., Malik, F. & Brown, D. Directional instability of microtubule
790 transport in the presence of kinesin and dynein, two opposite polarity motor
791 proteins. *J Cell Biol* **119**, 1589-96 (1992).
792 45. Kapitein, L.C. & Hoogenraad, C.C. Which way to go? Cytoskeletal
793 organization and polarized transport in neurons. *Mol Cell Neurosci* **46**, 9-20
794 (2011).

795 46. Che, D.L., Chowdary, P.D. & Cui, B. A close look at axonal transport: Cargos
796 slow down when crossing stationary organelles. *Neurosci Lett* **610**, 110-6
797 (2016).
798 47. Chowdary, P.D., *et al.* Nanoparticle-assisted optical tethering of endosomes
799 reveals the cooperative function of dyneins in retrograde axonal transport. *Sci*
800 *Rep* **5**, 18059 (2015).
801 48. Bilsland, L.G., *et al.* Deficits in axonal transport precede als symptoms in vivo.
802 *Proc Natl Acad Sci U S A* **107**, 20523-8 (2010).
803 49. Gennerich, A., Carter, A.P., Reck-Peterson, S.L. & Vale, R.D. Force-induced
804 bidirectional stepping of cytoplasmic dynein. *Cell* **131**, 952-65 (2007).
805 50. Lalli, G., Bohnert, S., Deinhardt, K., Verastegui, C. & Schiavo, G. The journey
806 of tetanus and botulinum neurotoxins in neurons. *Trends Microbiol* **11**, 431-7
807 (2003).
808 51. Morris, R.L. & Hollenbeck, P.J. Axonal transport of mitochondria along
809 microtubules and f-actin in living vertebrate neurons. *J Cell Biol* **131**, 1315-26
810 (1995).
811 52. Belyy, V., *et al.* The mammalian dynein-dynactin complex is a strong opponent
812 to kinesin in a tug-of-war competition. *Nat Cell Biol* **18**, 1018-24 (2016).
813 53. Cleary, F.B., *et al.* Tension on the linker gates the atp-dependent release of
814 dynein from microtubules. *Nat Commun* **5**, 4587 (2014).
815 54. Chereau, R., Saraceno, G.E., Angibaud, J., Cattaert, D. & Nagerl, U.V.
816 Superresolution imaging reveals activity-dependent plasticity of axon
817 morphology linked to changes in action potential conduction velocity. *Proc Natl*
818 *Acad Sci U S A* **114**, 1401-1406 (2017).

819 55. Duan, R., *et al.* Spectrin is a mechanoresponsive protein shaping fusogenic
820 synapse architecture during myoblast fusion. *Nat Cell Biol* **20**, 688-698 (2018).
821 56. Evans, M.D., Tufo, C., Dumitrescu, A.S. & Grubb, M.S. Myosin ii activity is
822 required for structural plasticity at the axon initial segment. *Eur J Neurosci* **46**,
823 1751-1757 (2017).
824 57. Taylor, A.M., *et al.* A microfluidic culture platform for cns axonal injury,
825 regeneration and transport. *Nat Methods* **2**, 599-605 (2005).
826 58. Harper, C.B., *et al.* Dynamin inhibition blocks botulinum neurotoxin type a
827 endocytosis in neurons and delays botulism. *J Biol Chem* **286**, 35966-76 (2011).
828 59. Persson, F., Linden, M., Unoson, C. & Elf, J. Extracting intracellular diffusive
829 states and transition rates from single-molecule tracking data. *Nat Methods* **10**,
830 265-9 (2013).
831 60. Monnier, N., *et al.* Inferring transient particle transport dynamics in live cells.
832 *Nat Methods* **12**, 838-40 (2015).
833

Acknowledgements

This work was supported by grants from the Australian Research Council (ARC, DP170102402 to VA; ARC DE170100546 to TW) and the Australian National Health and Medical Research Council (NHMRC; GNT1138452 to VA and GNT1120381 to FAM). FAM is an NHMRC Senior Research Fellow (GNT1060075). TW is an ARC DECRA Fellow (DE170100546) and was previously supported by a The University of Queensland Postdoctoral Research Fellowship. HH and XJY were recipients of University of Queensland Research Training Scholarships. Imaging was performed at the Queensland Brain Institute's Advanced Microscopy Facility, generously supported by the Australian Government through the ARC LIEF Grant (LE130100078 to FAM). Electron microscopy was performed at the Australian Microscopy and Microanalysis Facility, The University of Queensland. The authors would like to thank Rowan Tweedale for editing the manuscript, and Joanne Jang, Rumelo Amor, Nicholas Condon, Luke Hammond, Nick Valmas and Rachel Gormal for expert technical assistance.

Author contributions

FAM and TW designed the study, supervised the project and wrote the manuscript. TW performed live-imaging microscopy, confocal and SIM experiments and analysed data. WL performed HMM separation and assisted with data analysis. SM designed and performed EM experiments and helped with data analysis. AP designed and performed the analysis of particle speed and swap, and helped with SIM. GS helped to develop the staining protocol for dual-colour SIM. XJY and HH helped with primary neuronal culture, transfection, analysis of LC3-mRFP data. VA supervised works conducted by XJY, HH and WL, and edited the manuscript. VL and PP helped with the edition of the

858 manuscript and the figures. All authors discussed the results and commented on the
859 manuscript.
860
861 **Competing Interests**
862 The authors declare no competing interest.
863
864 **Materials & correspondence**
865 Correspondence and requests for materials should be addressed to Prof. Frederic A.
866 Meunier (f.meunier@uq.edu.au) and Dr Tong Wang (t.wang4@uq.edu.au).
867
868 **Data availability**
869 All other data supporting the findings of this study are available from the corresponding
870 authors upon reasonable request.

871

872 ***Figure legends***

873 ***Figure 1. The speed of retrograde axonal transport cargoes is inversely correlated***
874 ***with their size.***

875 **(a)** Microfluidic chambers to isolate unidirectional axon bundles, bar =1 cm (adapted
876 from Xonamicrofluidics.com). (**b)** Schematic diagram of the pulse-chase labelling
877 process. Cultured hippocampal neurons were grown in a microfluidic device for 14
878 days *in vitro* (DIV). The nerve terminal chamber was incubated with fluorescently
879 tagged CTB (50 ng/ml) for 5 min or Lysotracker Deep Red (50 nM) for 30 min (pulse).
880 After thorough washes and a 2h chase. (**c)** Representative images of cultured neurons,
881 showing the restriction of retrograde CTB surface labelling to nerve terminals and the
882 position of the observation window (white box). Scale bar = 50 μm. **(d)** The axonal
883 retrograde transport of CTB or Lysotracker was monitored, at the level of the proximal
884 axon shafts or in the nerve terminal chamber, respectively. (**e)** Time-lapse images of
885 CTB carriers. Top panels: CTB labelling and tracing trajectories within the axon
886 channels. Trajectories of small (#1, diameter ≤ 0.5 μm) and large (#2, diameter > 0.5
887 μm) carriers are magnified in the bottom panels, respectively. (**f)** Representative
888 kymographs of CTB-positive cargoes along a single axon, depicting track
889 displacements of small and large carriers. x-bar = 10 μm; y-bar = 10 s. (**g)** Grouped
890 analysis of the average speeds of CTB cargoes with small (diameter ≤ 0.5 μm) and
891 large (diameter > 0.5 μm) diameters. Data represent mean ± s.e.m (small, n=187, large
892 n=185 tracks from 3 independent preparations; two-tailed unpaired t-test, ***p<0.001).
893 (**h)** Pearson's coefficient of the speed and diameter of retrograde Lysotracker-positive
894 and CTB-positive cargoes. Data represent mean ± s.e.m from 3 independent
895 preparations (random, n=3 simulated data sets; Lysotracker, n=6 ; CTB, n=14; n

represents the number of axon channels analysed; the single value of the average correlation coefficient between the size and speed of all trajectories in each axon channel was calculated and used for the plot. 3 Independent groups of Gaussian-distributed random numbers were generated using the *normrnd* function of Matlab. Two-tailed unpaired t-test, **p<0.01, *p<0.05).

Figure 2. The size of axonal cargoes correlates with the diameter of the axon.

(a) Brightfield image of DIV14 rat hippocampal neurons cultured in a microfluidic device with the region selected for EM outlined. Scale bar = 250 μm. (**b)** Representative electron micrographs showing the axonal diameter measurements with cargo (red) or without cargo (blue), and the associated cargo size (white). Scale bar = 0.5 μm **(c)** Electron micrographs of axon bundles from hippocampal neurons cultured in microfluidic devices. (**i-iv)** Axon diameters with and without cargo are marked with red and blue arrows, respectively. (**i)** Endosome = black arrow, (**i-iii)** Mitochondria = white arrowheads, autophagosome = black arrowheads. (**iv)** Inner diameters of cargoes are marked with white arrows. Bars = 500 nm. (**d)** Quantification of axon diameters with cargo and without cargo. Data represent mean ± s.e.m, n= 182 (+ Cargo) and 182 (- Cargo) measurements from 2 independent preparations (two-tailed paired t-test, ***p<0.001). (**e)** Grouped quantification of axonal diameter as a function of binned vesicle size. Data represent mean ± s.e.m; for the + Cargo group from left to right: n=104, 23, 41 and 14 measurements; for the - Cargo group from left to right: n=104, 23, 41 and 22 measurements, data were from 2 independent preparations (two-tailed unpaired t-test, *p<0.05; ***p<0.001). (**f)** Cross-correlation analysis of cargo size and axonal diameter. Linear regressions were performed with the 182 paired measurements

of axonal and cargo diameters of the (+ Cargo) group, data from 2 independent preparations.

Figure 3. Large retrograde cargoes produce "black-holes" within the axons of Lifeact-GFP-expressing neurons.

(a) Rat hippocampal neurons transfected with Lifeact-GFP were pulse-labelled with CTB for 5 min and immediately subjected to 2D-SIM imaging; boxed regions of axonal segments are shown on the right. Relative localization of plasma membrane (CTB-labelled, arrowheads), F-actin (Lifeact-GFP; asterisk) and cytosolic actin (Lifeact-GFP; arrows). Bar = 10 μm (right), 1 μm (left). (**b)** Rat hippocampal neurons were transfected with Lifeact-GFP and imaged with 3D-SIM. Top: a representative maximum projection of 3D-SIM of Lifeact-GFP expressing axons are shown; Bar = 5 μm. Bottom: magnified regions of interest (ROIs) in top panel, arrowheads indicate black-holes with low Lifeact-GFP signals within the axon. Bar = 1μm. (**c)** Quantification of axon diameters with (+) and without (-) black-holes. Data represent mean ± s.e.m from 3 independent preparations (+ black-hole, n=29, - black-hole, n=29 axons; two-tailed unpaired *t*-test, ***$p<0.001$). (**d-e)** Cultured hippocampal neurons grown in a microfluidic device were transfected on DIV12 with Lifeact-GFP and co-transfected with either LC3-mRFP (autophagosome) (**d)**, Rab7-mRFP (late endosome) (**e)** or Mito-TagRFP (mitochondria) (**f)**, and subjected to time-lapse imaging on DIV 14. Representative dual-colour 3D-SIM projections of neurons expressing Lifeact-GFP and with different subcellular markers are magnified in right panels, and overlapping regions are annotated. Bar = 5 μm. (**g)** Quantification of axon diameters with (+) and without (-) annotated markers. Data represent mean ± s.e.m (n=10 axons for each marker from 3 independent cultures; two-tailed unpaired t-test, **$p<0.01$; ***$p<0.001$). (**h-i)** Representative dual-colour

945 3D-SIM projections of axons expressing Lifeact-GFP, which were co-labelled with the
946 retrograde cargo marker CTB (**h**) or DIC[1B] (**i**). Boxed regions are magnified in right
947 panels, overlapping regions are annotated. Bar = 2 μm (**h**) and 5 μm (**i**).
948
949 ***Figure 4. The transit of cargo causes a transient radial expansion of the axon.***
950 **(a)** Rat hippocampal neurons cultured in a glass-bottom dish were transfected with
951 Lifeact-GFP (DIV 12) and imaged by time-lapse SIM (DIV 14). Representative live
952 axons with cargo-associated black-holes passing through are shown, with inset
953 demonstrating the Gaussian fittings of the annotated line transection of axon. Bar = 0.5
954 μm (inset). (**b**) Time-lapse images of bracketed region in A, showing the axonal
955 diameter fluctuation as the cargo (indicated with red bar) transits. (**c**) Plot of the distance
956 between axon membranes against time. (**d-e**) Live-confocal imaging of axons carrying
957 CTB-positive (**c**) or Lysotracker-positive (**d**) cargoes. Magnified images of the boxed
958 region are shown in the lower panels, and moving cargoes are indicated with
959 arrowheads. Bar = 10 μm.
960
961 ***Figure 5. Short-term inactivation of NM-II increases the axon diameter without***
962 ***affecting the actin ring periodicity.***
963 **(a)** SIM images of a Lifeact-GFP-expressing axon from a DIV14 rat hippocampal
964 neuron, before and after short-term blebbistatin treatment (10 μM, 60 min). Boxed
965 regions are magnified in right panels. Axon diameter with and without cargoes is
966 indicated by arrowheads and arrows respectively. Bar = 0.4 μm. (**b**) Axon diameter
967 quantification. Data represent mean ± s.e.m, n=29, 29, 37, 37 axons from left to right.
968 Values were measured from 3 independent cultures (two-tailed unpaired t-test,
969 ***p<0.001) (**c**) Analysis of axon diameter fluctuation. Data represent mean ± s.e.m,

n=29 (pre), 22 (+BLB) axons from left to right. Values were measured from 3 independent cultures (two-tailed unpaired t-test, ***p<0.001). (**d)** SIM images of endogenous F-actin (phalloidin) along the axon of a DIV14 rat hippocampal neuron before and after short-term blebbistatin treatment (10 µM, 60 min). Bracketed regions are magnified on the right, and the diameters of actin rings are shown below. (**e, f)** Comparison of periodic actin spacing distribution (**e)** and average value (**f)** in control and blebbistatin-treated neurons. Data represent mean ± s.e.m, n=300 (Control), 316 (+BLB) for periodicity quantification. (**g)** Autocorrelation analysis of the actin periodicity of control and blebbistatin-treated axons. Data represent mean ± s.e.m, n = 10 (Control) and 8 (+BLB) axon segments were measured. (**h)** Distribution of actin diameters in control and blebbistatin-treated axons. Data represent mean ± s.e.m, n = 42 (Control) and 46 (+BLB) actin rings diameters were measured. (**i)** Quantification of actin ring diameter fluctuations; the diameters per 10 µm axon segments were measured and quantified. Data represent mean ± s.e.m, n=11 (Control) and 11 (+BLB) axon segments were analysed. Values were measured from 3 independent cultures (two-tailed unpaired t-test, n.s. no significant difference; **p<0.05; ***p<0.001).

Figure 6. NM-II immunostaining reveals a periodic pattern that correlates with the periodic actin rings along the axons.

(a) Dual-colour SIM images of endogenous F-actin (phalloidin) and NM-IIB in control and blebbistatin-treated axons of DIV14 rat hippocampal neurons. Boxed regions are magnified in right panels. Bar = 1 µm (left) and 0.5 µm (right). Discrete distributions of NM-II and actin are marked with arrows in bottom panels. (**b)** A line profile was used to characterize the periodic actin ring and NM-II structures. Overlapping and alternating peaks are marked with arrows and arrowheads respectively. (**c-e)**

Comparison of NM-II distribution in control and short-term (60 min) blebbistatin-treated axons. Due to the staining efficiency of the NM-II antibody, only the spacing between at least 4 consecutive NM-II puncta were analysed. The Gaussian distribution (**c)** autocorrelation (**d)** and scattered plot (**e)** of NM-II spacing are shown. Data represent mean ± s.e.m, n = 8 (pre) and 9 (+BLB) axon segments were analysed for autocorrelation; n = 262 (Control), 261 (+BLB) NM-II puncta were analysed for periodic distribution. Data are from 3 independent cultures (two-tailed unpaired t-test, n.s. no significant difference). (**f)** Comparison of NM-II and actin ring cross-correlation in control and short-term (60 min) blebbistatin-treated axons; significant reduction of cross-correlation after blebbistatin treatment is annotated at 0 nm shifts. Data represent mean ± s.e.m; n = 5 (Control), 6 (+BLB) axon segments were analysed. Values were from 3 independent cultures (two-tailed unpaired t-test, ***p<0.001).

Figure 7. Short-term inactivation of actomyosin-II reduces the efficiency of retrograde axonal trafficking.

(a) DIV 14 rat hippocampal neurons were cultured in microfluidic devices, and the axon segments were subjected to short-term blebbistatin treatment (10 µM, 60 min). Trajectories of CTB-positive cargoes in the axon channels were traced before (pre) and after (+BLB) blebbistatin treatment. Bar = 10 µm. (**b, c)** Track speed (trajectory length/duration) of the CTB carriers (**b)** or Lysotracker carriers (**c)** before (pre) and after (+BLB) blebbistatin treatment. The speeds of these carriers were sub-grouped according to their diameters. Data represent mean ± s.e.m, n=187, 185, 271, 286 (CTB) and n=179, 342, 128, 573 (Lysotracker) trajectories from 3 independent cultures (two-tailed unpaired t-test, *p<0.05, ***p<0.001, n.s. no significant difference). The same data of pre-treated groups were used in Figure 1G and Figure S1B. (**d)** Displacement-

time plot of representative CTB trajectories. (i) Fast moving state, and (ii) stalled state, as magnified on the right, with the back-and-forth movements marked with asterisks. x-bar = 10 µm, y-bar= 20 s. (**e)** Time ratio of cargo travelling in the reverse direction (swap) to total time travelled. Data represent mean ± s.e.m, n=28 (Pre) and 34 (+BLB) channels from 3 independent preparations (two-tailed unpaired t-test, ***p<0.001). (**f)** Quantification of the frequency of CTB-labelled vesicles that cross the observation window per minute. Data represent mean ± s.e.m, n = 51 (Pre) and 32 (+BLB 60') channels from 3 independent preparations (two-tailed unpaired t-test, *p<0.05). (**g)** CTB trajectory displays stalled (D, blue) and fast-moving (DV, pink) motion states inferred by HMM-Bayes analysis. Example of an annotated trajectory colour-coded with the indicated motion states. The time line shows the temporal (s) sequence of the inferred D and DV motion states. (**h)** Step sizes of the two motion states before (pre) and after (+BLB) blebbistatin treatment. Data represent mean ± s.e.m, from left to right, n= 126, 126, 190, 190 different trajectories from 3 independent preparations (two-tailed unpaired t-test, ***p<0.001).

Figure 8. Long-term inhibition of actomyosin-II activity triggers accumulation of stalled cargo in focal axonal swellings (FAS).

(**a)** Hippocampal neurons (DIV 14) expressing Lifeact-GFP were incubated with blebbistatin (10 µM) for the indicated durations. Time-lapse SIM images showing morphological changes. The bracketed regions are magnified. Bar = 2 µm (left); 1 µm (right). (**b)** Percentage of axons with FAS following short-term (60 min) and long-term (120 min) blebbistatin treatment. Data represent mean ± s.e.m, n=10 (Pre), 9 (+BLB, 60 min) and 10 (+BLB, 120 min) independent ROIs were analysed. (**c-e)** Representative channel overlapping with CTB trajectories is shown in (**c)**. Quantification of the track

speed (**d)** and transverse frequency (**e)** of CTB carriers following long-term (120 min) blebbistatin treatment. Bar = 10 μm. Data represent mean ± s.e.m; for track speed analysis, n=185 (Pre), 286 (60 min) and 215 (120 min) trajectories, the same data sets of large cargo speed in pre-treated groups were used in Fig. 1g and Fig. 7b; for frequency analysis, n=51 (pre), 32 (60 min) and 13 (120 min) independent channel ROIs were analysed. (**f)** DIV 14 hippocampal neurons expressing Lifeact-GFP and LC3-mRFP were incubated with blebbistatin (10 μM, 120 min), with the accumulated autophagosome cargoes marked by asterisks. Kymograph of an axon is shown in the bottom panel. x-bar = 10 μm, y-bar = 60 s. (**g)** Quantification of the average speed of LC3 cargoes, and the number of FAS accompanied with LC3 cargo accumulation (**h)**, following long-term blebbistatin treatment. Data represent mean ± s.e.m; for LC3 speed, n= 72 (Pre), n=68 (120 min) trajectories; for the FAS percentage, n=10 (Pre), 9 (120 min) independent ROIs. All data were from 3 independent cultures (two-tailed unpaired t-test, *p<0.05; ***p<0.001). **(i)** Rat hippocampal neurons were co-transfected on DIV12 with the Lifeact-mRFP and either myosin-II regulatory light chain wild-type or S19AT18A mutant (MRLC^{mut}-GFP) plasmids. On DIV14 the diameter fluctuations **(j)** and FAS numbers per μm **(k)** of transfected axons were quantified. Data represent mean ± s.e.m; for actin ring fluctuation **(j)**, n= 25 (wt), n=45 (mut) independent axonal segments are measured; for the FAS counts **(k)**, n=9 (wt), 26 (mut) independent axons are counted. Data were from 2 independent preparations (two-tailed unpaired t-test, ***p<0.001).

Supplementary information

Supplementary Figure 1. The speed of Lysotraker-positive cargoes is inversely correlated with their size in axons of cultured hippocampal neurons.

(a) Representative time-lapse images of Lysotracker carriers at the nerve terminals of DIV 14 rat hippocampal neurons. Top-left: Lysotracker labelling at nerve terminals as isolated by the device. Top-right: Imaris tracing trajectories of the same region of interest. Trajectories of small (1#, diameter ≤0.5 μm) and large (2#, diameter > 0.5 μm) carriers were magnified in the bottom panels respectively. (**b)** Grouped analysis of average speeds of Lysotracker-positive cargoes with small (≤0.5 μm) and large (> 0.5 μm) diameters, showing a significant difference. Data represent mean ± s.e.m from 3 independent preparations (small, n=179, big n=342 tracks; two-tailed unpaired t-test, ***p<0.001). The same data sets were also used in the pretreated group of Figure 7C.

Supplementary Figure 2. Periodic distribution of F-actin rings along the axon of hippocampal neurons.

(a) DIV14 rat axons were stained for endogenous F-actin (phalloidin) and imaged with 3D-SIM; two different boxed regions magnified with maximum z-projections shown in the lower panels. Axon diameters were measured as the average of a 1 μm segment. **(b)** Periodic actin peaks were identified using the 'find peak' function of BAR collection in Image J (SMA=1), along the line profiles as shown with dashed lines in 1# of **(a)**. x-value of the peaks were extracted, and the distance between adjacent peaks was shown in Fig. 5f, in both untreated (control) or short-term (60 min) blebbistatin-treated axons. **(c)** Hippocampal neurons transfected at DIV12 with Lifeact-GFP and imaged with 3D-SIM on DIV 14, comparison of wide-filed and SIM images are made. Bracketed regions are amplified in the lower panels. **(d)** Amplification of the boxed regions in **(c)**, periodic

actin rings are indicated with arrows. Bar=0.5 μm. **(e)** line profile of **(d)**, showing the periodicity of the actin peaks. **(f)** More representative cases showing the periodic actin rings using Lifeact-GFP transfected neurons. **(g)** Distribution of actin ring spacing. Data represent mean ± s.d., n=251 actin peaks for periodicity quantification. Values were measured from 3 independent cultures.

Supplementary Figure 3. NM-II immunostaining reveals a periodic pattern that correlates with the periodic actin rings along the axon.

(**a)** DIV14 rat hippocampal neurons was stained for endogenous F-actin (Phalloidin) and NM-IIB and imaged with dual-colour 3D-SIM, boxed regions are magnified with individual z-stack planes shown, periodic structure of NM-II and actin are indicated with arrows (green) and spots (red) respectively. **(b)** The NM-II and actin structures resolved with 3D-SIM (right) were rendered into surface (right) using Imaris; boxed regions are magnified to show the accuracy of the rendering. The colocalization of the bracketed region is shown in the bottom panels. **(c)** Comparison of colocalization between NM-II and actin rings before and after the 60 min blebbistatin treatment. Bar= 0.5 μm. **(d)** The Manders coefficient reflecting the colocalization rate. Data represent mean ± s.e.m, n=30 (-BLB), 30 (+BLB) axon segments for fraction of the F-actin overlapping with NM-II; data were from 3 independent cultures (two-tailed unpaired t-test, $^{**}p<0.01$). **(e)** Two-colour SIM images of endogenous F-actin (phalloidin) and NM-II along the axons of control and Triton X-100-extracted axons. Bar = 1 μm. (**f-h)** Quantification of the percentage of axons bearing periodic actin rings (**f)**, NM-II puncta number **(g)**, and the percentage change in these two parameters **(h)** in control and Triton X-100-extracted axons (+Triton). Data represent mean ± s.e.m, n=10 cells (Control)

and 9 cells (Triton X-100) from 3 independent cultures (two-tailed unpaired t-test, $^{**}p<0.01$; $^{***}p<0.001$).

Supplementary Figure 4. Periodic NM-II filaments are perpendicular to the longitudinal axis of the axon.

(a) DIV 14 hippocampal neurons were stained with the antibody against the C-terminal of NM-IIB (αNM-IIB(ct)). Representative 3D-STED images showing the periodic NM-II filaments in two different ROIs (1# and 2#). Bracketed regions are amplified with NM-II filaments were marked out in the right panels, double arrows annotate the direction of axonal longitudinal axis, single NM-II filament is amplified in bottom panels with the angle to the longitudinal axis marked out. Bar=300 nm (right panels for 1# and 2#). **(b-c)** The quantification of the angle between NM-II filament and the axonal axis **(b)** and the periodic spacing between NM-II filaments. Data represent mean ± s.e.m, n=212 NM-II filaments from 3 independent cultures, R^2=0.982 **(b)**. R^2=0.994 **(c)**. **(d)** Schematic showing the dual-antibody labelling assay using both antibodies recognizing the C-terminus (αNM-IIB(ct)) and N-terminus (αNM-IIB(nt)) of NM-IIB filaments. **(e)** representative 3D-SIM images of the dual-antibody labelling assay, with two dual-stained NM-IIB filaments amplified in the right panels. Double arrow indicates the direction of axon axis.

Supplementary Figure 5. Short-term inactivation of NM-II causes the axon diameter expansion without affecting the microtubule structure or docking mitochondria.

(a) Schematic cartoon showing the structure of a 6-well microfluidic device. (**b)** Time-lapse images showing the distribution of Af488 dye in the middle chamber of a 6-well microfluidic device, indicating its restriction capacity. Bar = 50 μm. (**c)** Axons of DIV

14 hippocampal neurons were treated with blebbistatin (10 μM) in the middle chamber for 90 min. Representative images of the 3D-SIM time-lapse images of axons before (Pre) and after blebbistatin treatment (+BLB). Value of z-axis is colour-coded. Scale Bar = 5 μm. Magnified images from the boxed regions and the corresponding Imaris surface rendered images are shown in panels on the right. Bar=1 μm. (**d-e)** Quantification of changes in the axon diameter (**d)** and volume (**e)** before and after blebbistatin treatment. Data represent mean ± s.e.m, for diameter quantification n=10 (Pre) and 10 (+BLB) axons were analysed, for volume quantification n = 8 axons (Pre) , n = 8 (+BLB) axons were analysed, from 3 independent cultures (two-tailed paired t-test, ***p<0.001). (**f)** DIV 14 hippocampal neurons were treated with blebbistatin (10 μM, 60 min), then fixed and stained for endogenous F-actin (phalloidin) and β-III-tubulin. Two-colour SIM was used to resolve the actomyosin and microtubule structures, respectively. Bar = 1 μm. Quantification of changes in the microtubule intensity (**g)** and bundle width (**h)** in control and blebbistatin-treated one. Data represent mean ± s.e.m, for intensity quantification n=33 (Pre) and 34 (+BLB), for bundle width quantification n = 33 axons (Pre), n = 37 axons (+BLB), from 3 independent cultures (two-tailed paired t-test, n.s. no significant difference). **(i)** Hippocampal neurons transfected with mito-TagRFP (red) and Lifeact-GFP (green) were imaged at the level of their axons before and after blebbistatin treatment. Kymograph of mitochondria movements from boxed regions are shown in lower panels. Asterisks indicate moving mitochondria. xBar=10 μm, yBar=10 s. **(j)** Quantification of average speed of mitochondria transport in **(i**). The frequency distribution of the trajectories with different speed are shown to note the effect on docking (0 and 0.1 μm/s) and moving mitochondria. Data represent mean ± s.e.m, n=7 (Pre) and 8 (+BLB) axons from 3 independent cultures (Student's t-test, *p<0.05). **(k)** Quantification of average speed of

CTB-positive carriers with and without blebbistatin treatment, as shown in transport in **(Fig. 7a**). The frequency distribution of the trajectories with different speed are shown to note the effect on slow and fast CTB-carriers, respectively. Data represent mean ± s.e.m, n=3 (Pre) and 3 (+BLB) experiments from 3 independent preparations (Student's t-test, *p<0.05).

Supplementary* Movie 1. *Retrograde trafficking of Lysotracker-labelled cargoes in the axon terminals.

The retrograde trafficking of axonal cargoes labelled with Lystotracker-deepRed in the terminal chamber of the microfluidic device. From top to bottom: The Lysotracker carriers overlapping with bright field signals and the masked carriers and trajectories are shown in the top panels, with the boxed regions of interest being magnified in the bottom panels. Bar = 5 µm.

Supplementary* Movie 2. *Retrograde trafficking of CTB-labelled endosomes.

The retrograde trafficking flux of axonal cargoes labelled with CTB in an axon channel of a microfluidic device. From top to bottom: the CTB-labelled cargoes, their trajectories, and the trajectories that overlapped with the brightfield signals are shown, respectively. Bar = 5 µm.

Supplementary Movie 3. The transit of cargo causes a transient radial expansion of the axon.

The passage of cargoes-associated black-holes through the axon shafts caused an obvious mechanical stretching of the shafts, which are visualized in the Lifeact-GFP-expressing neuron (green) by time-lapse SIM. Black-holes that associated with moving

cargoes are indicated with arrows. Bar = 2 µm.

Supplementary Movie 4. Retrograde trafficking of CTB-labelled endosomes with short-term blebbistatin treatment.

The retrograde trafficking flux of axonal cargoes labelled with CTB in an axon channel of a microfluidic device, after treatment with 10 µM blebbistatin for 60 min. From top to bottom: the CTB-labelled cargoes, their trajectories and the trajectories that overlapped with the brightfield signals were shown, respectively. Bar = 5 µm.

Supplementary Movie 5. Retrograde trafficking of Lysotracker-labelled endosomes after blebbistatin treatment.

The retrograde trafficking of axonal cargoes labelled with Lystotracker-deepRed in the terminal chamber of a microfluidic device, after treated with 10 µM blebbistatin for 60 min. From top to bottom: the Lysotracker carriers overlapping with bright field signals and the masked carriers and trajectories are shown in the top panels, with the boxed regions of interest being magnified in the bottom panels. Bar = 5 µm.

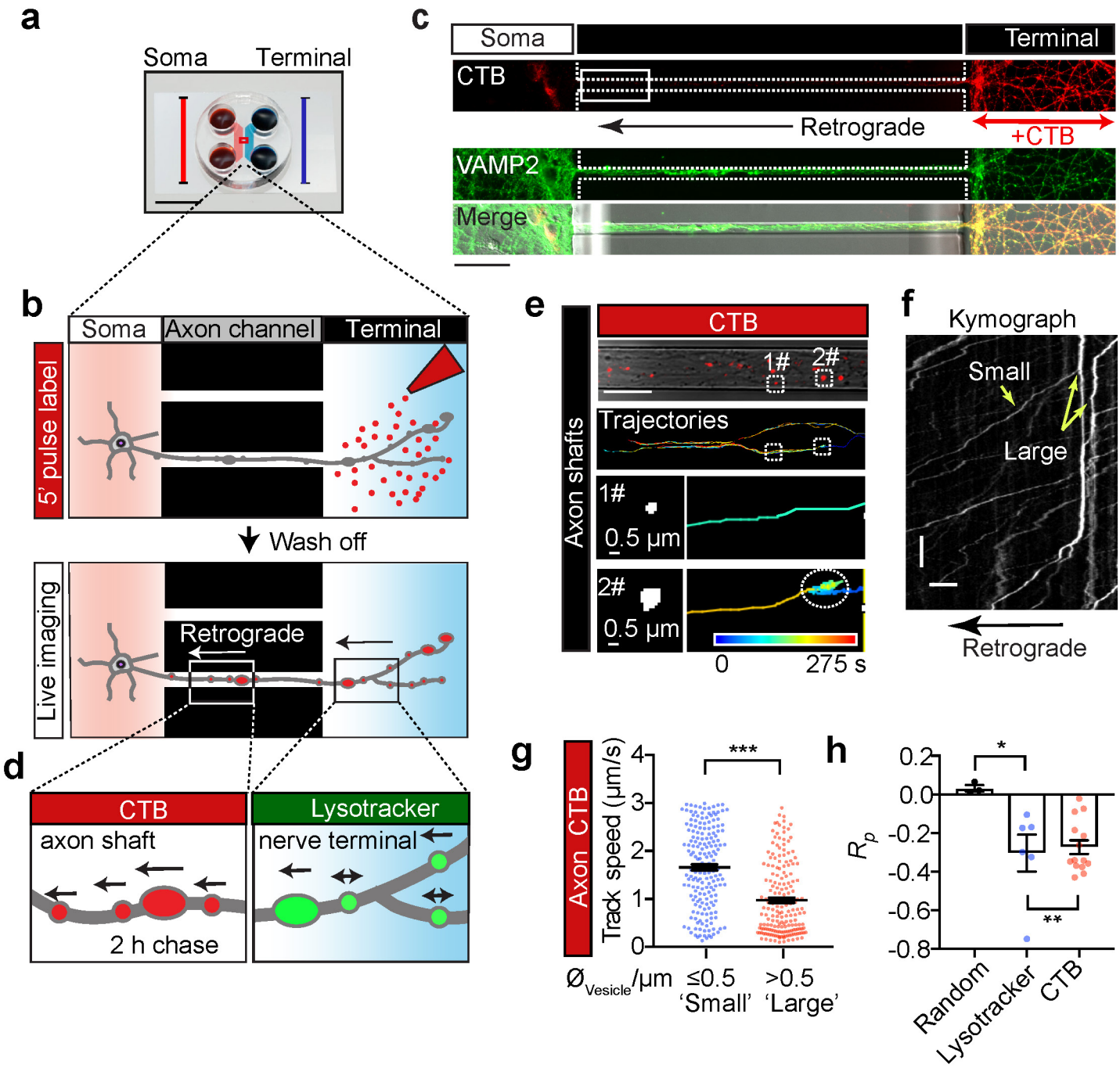

Figure 1. The speed of retrograde axonal transport cargoes is inversely correlated with their size.

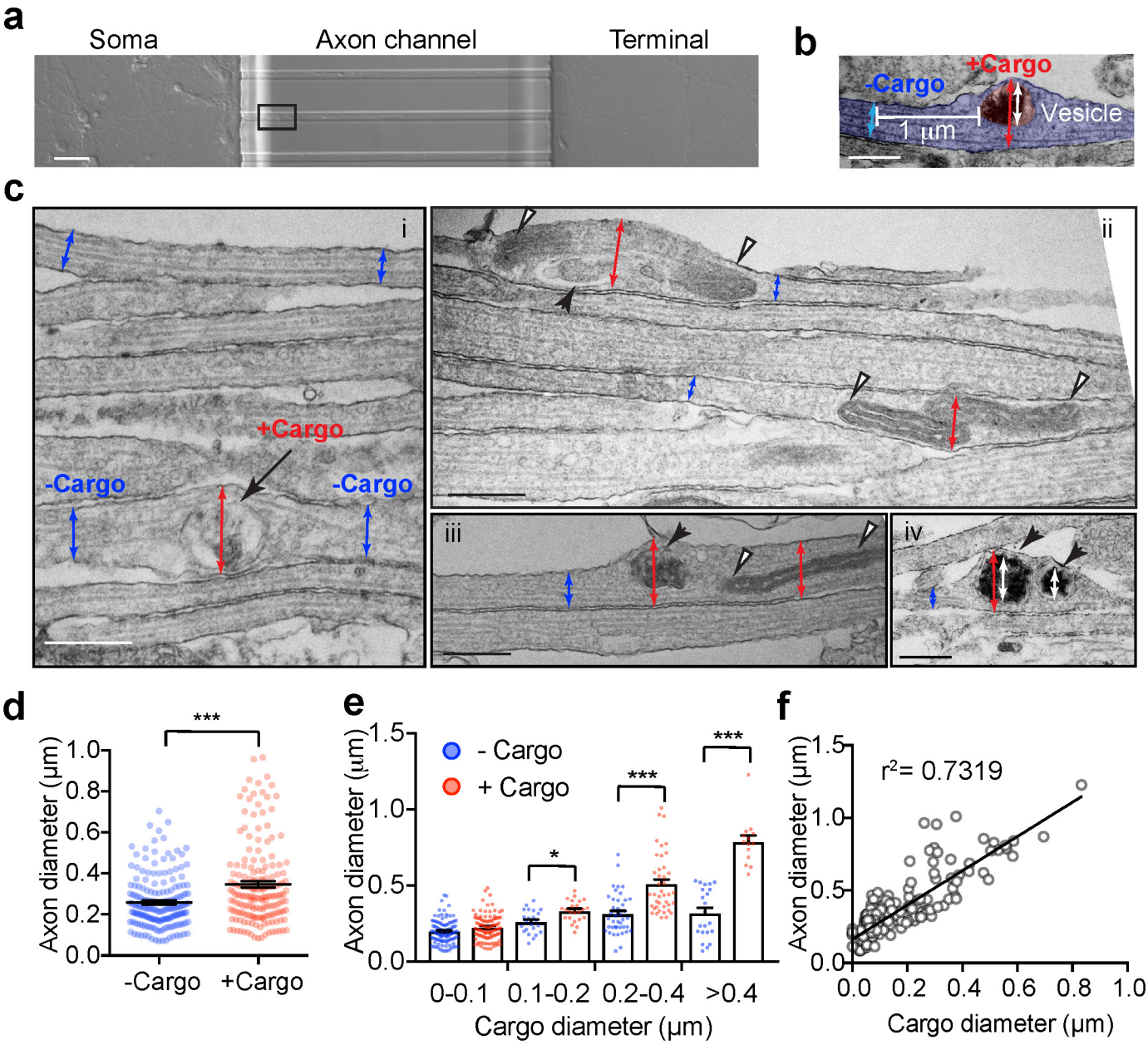

Figure 2. The size of axonal cargoes correlates with the transient radial expansion of axon shafts.

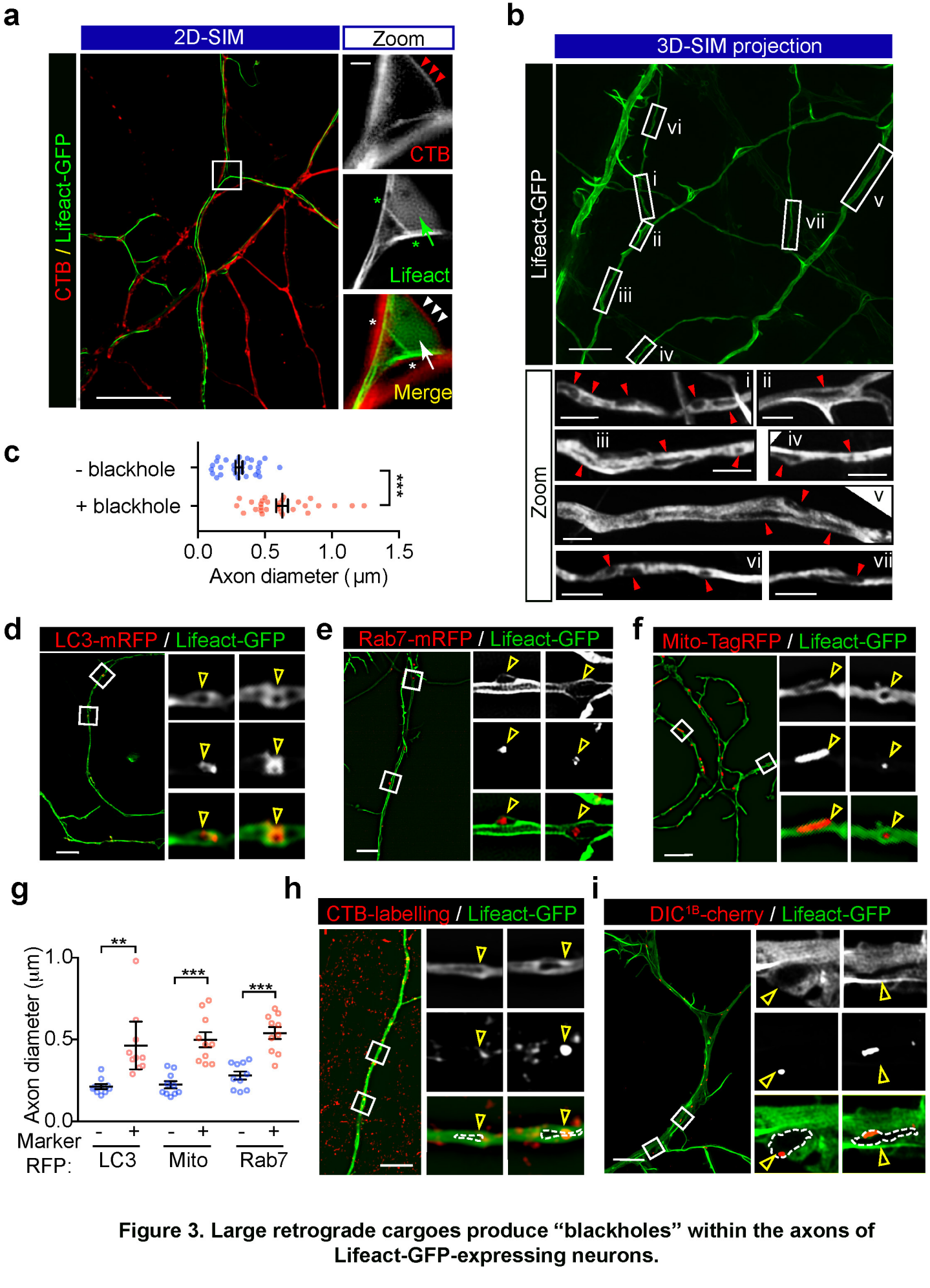

Figure 3. Large retrograde cargoes produce "blackholes" within the axons of Lifeact-GFP-expressing neurons.

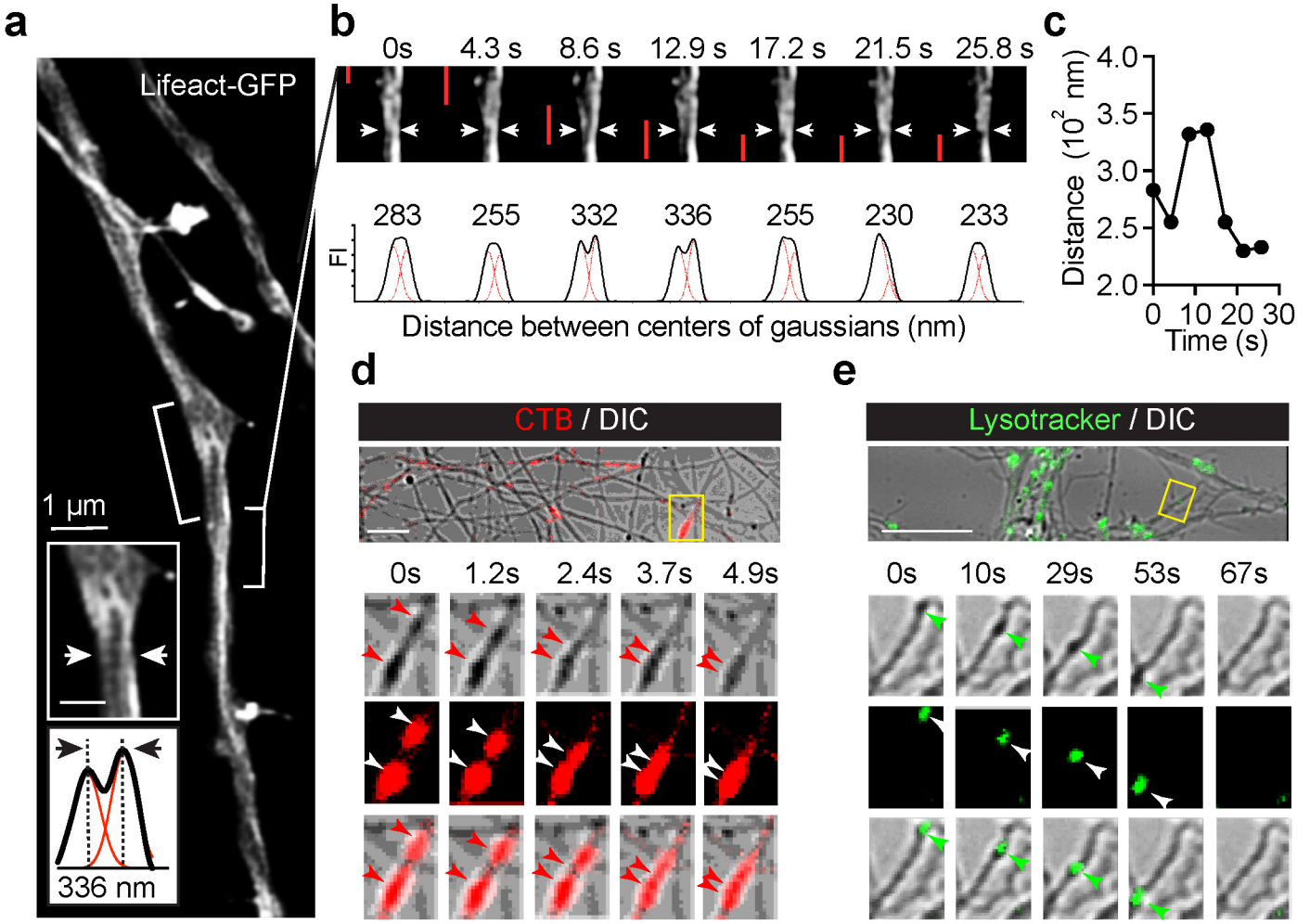

Figure 4. The transit of cargo causes a transient radial expansion of the axon.

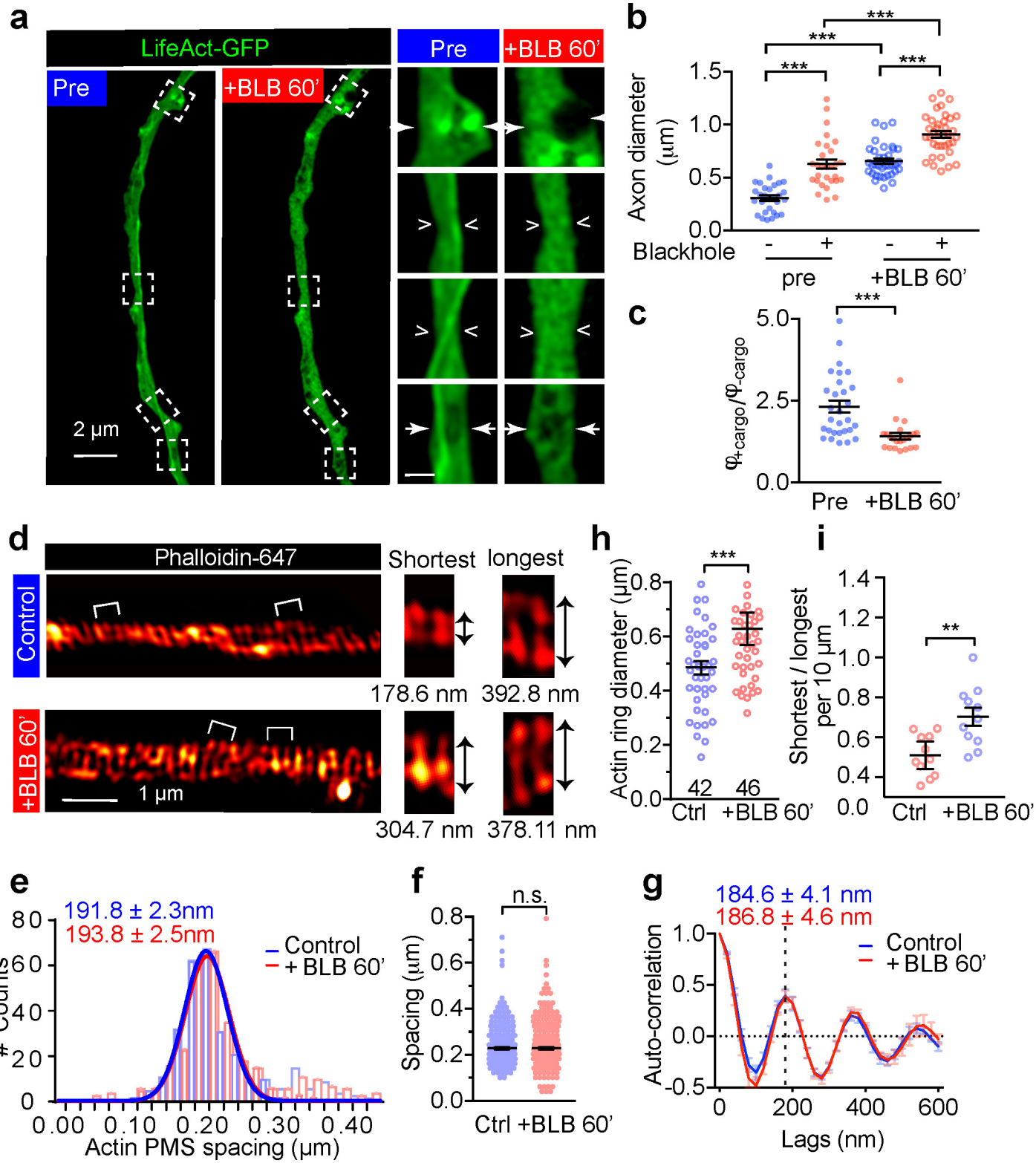

Figurer 5 Short-term inactivation of NM-II increases the axon diameter without affecting the actin ring periodicity.

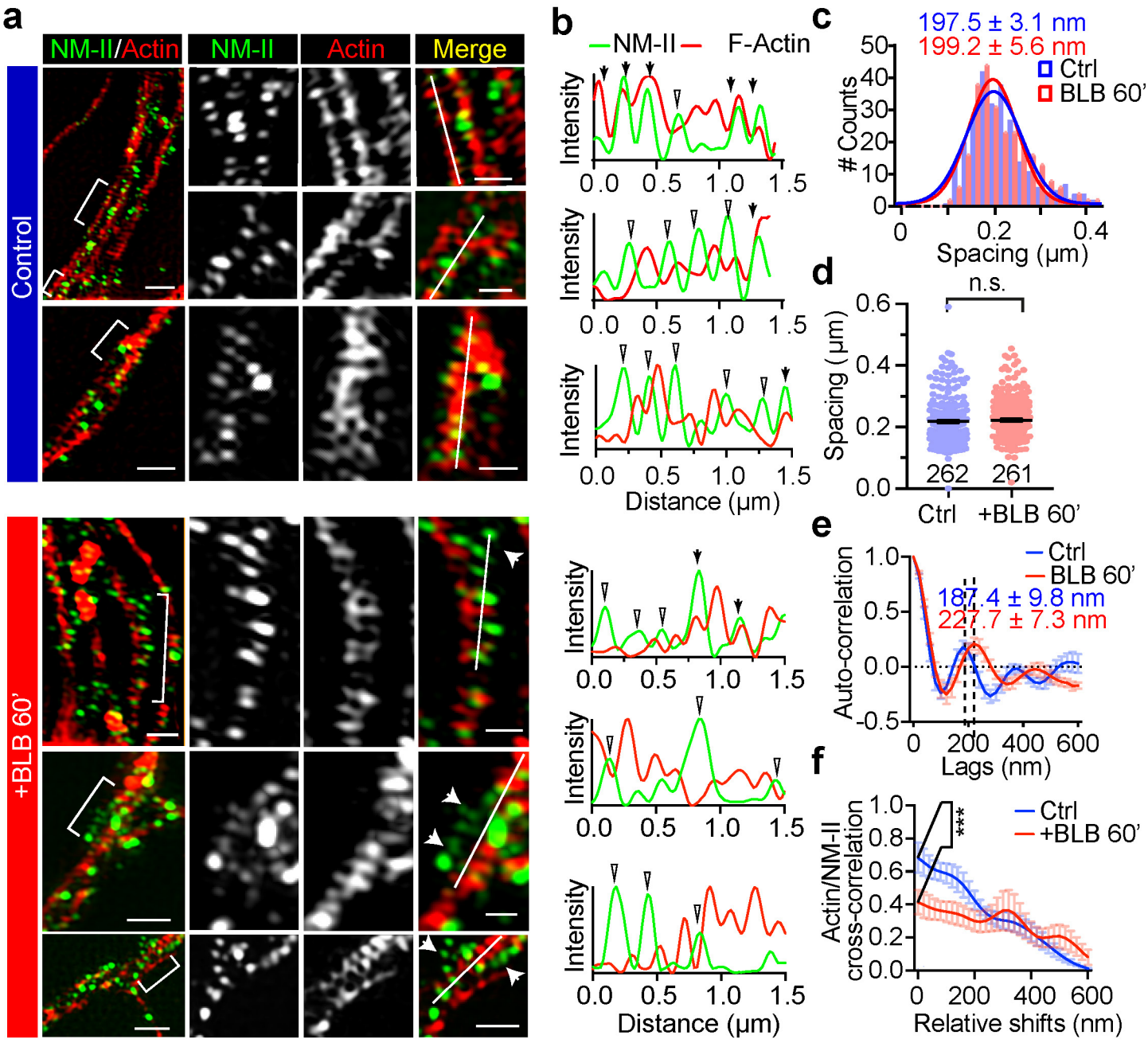

Figure 6. NM-II immunostaining reveals a periodic pattern that correlates with the periodic actin rings along the axons.

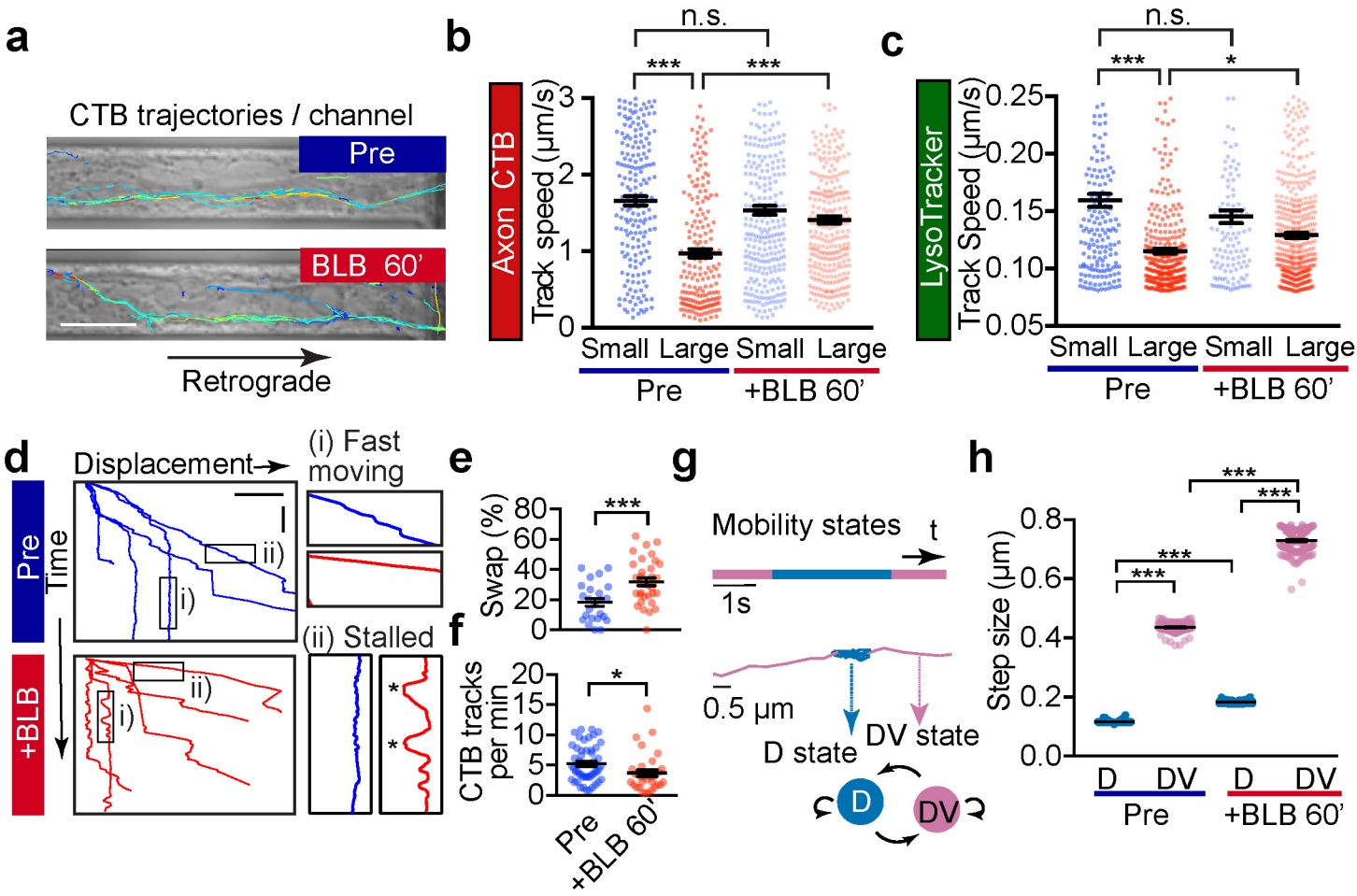

Figure 7. Short-term inactivation of actomyosin-II reduces the retrograde transport efficiency.

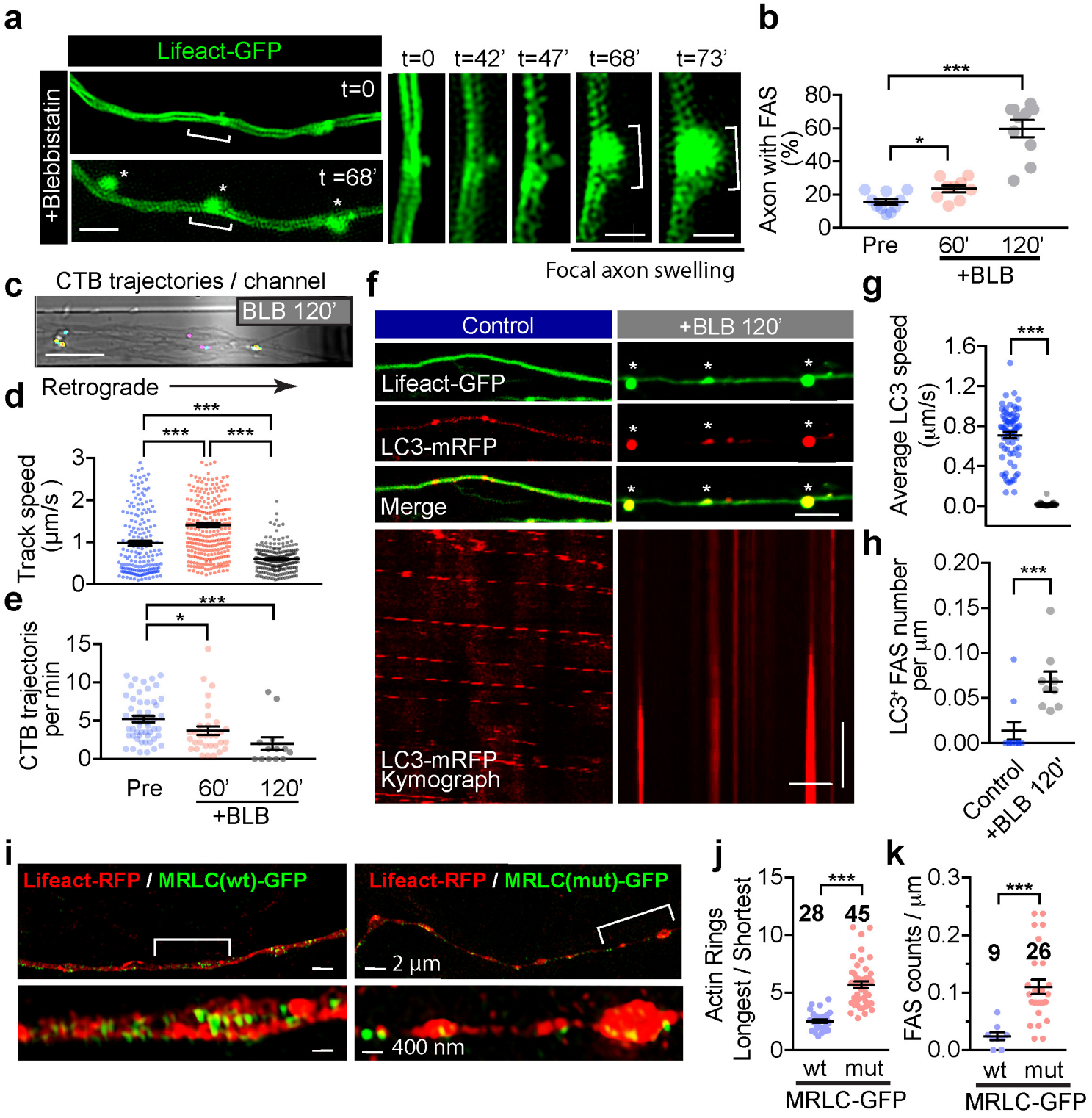

Figure 8. Long-term inhibition of actomyosin-II activity triggers accumulation of stalled cargo in focal axonal swellings (FAS).

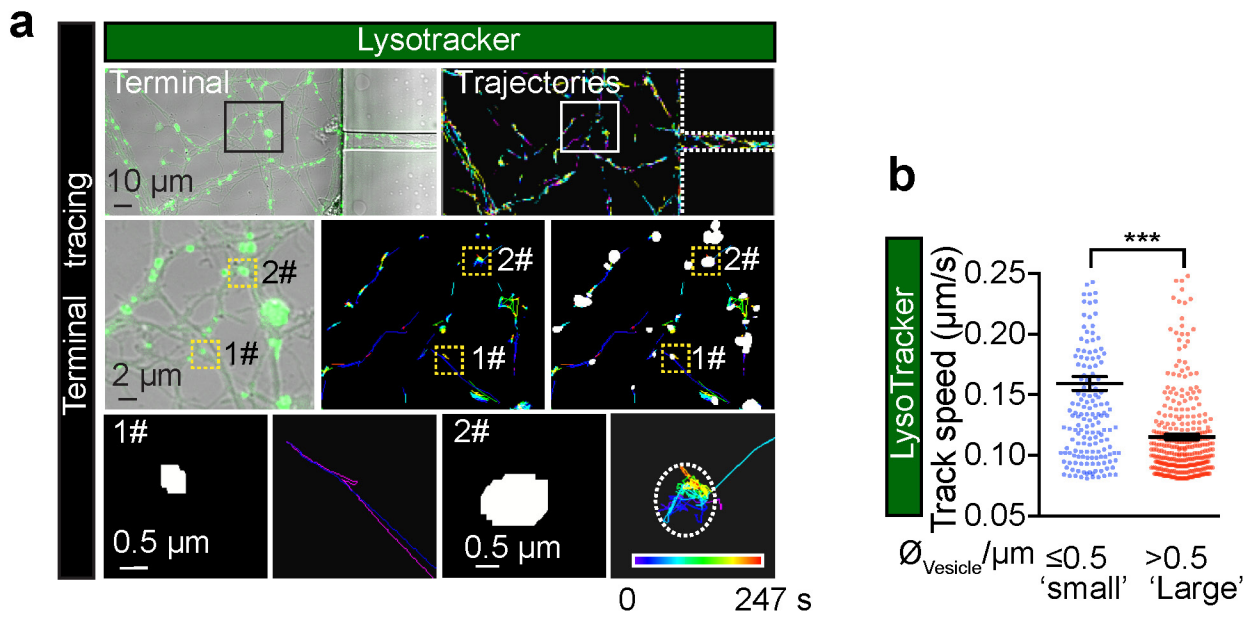

Supplementary Figure 1. The speed of Lysotracker-positive cargoes is inversely correlated with their size.

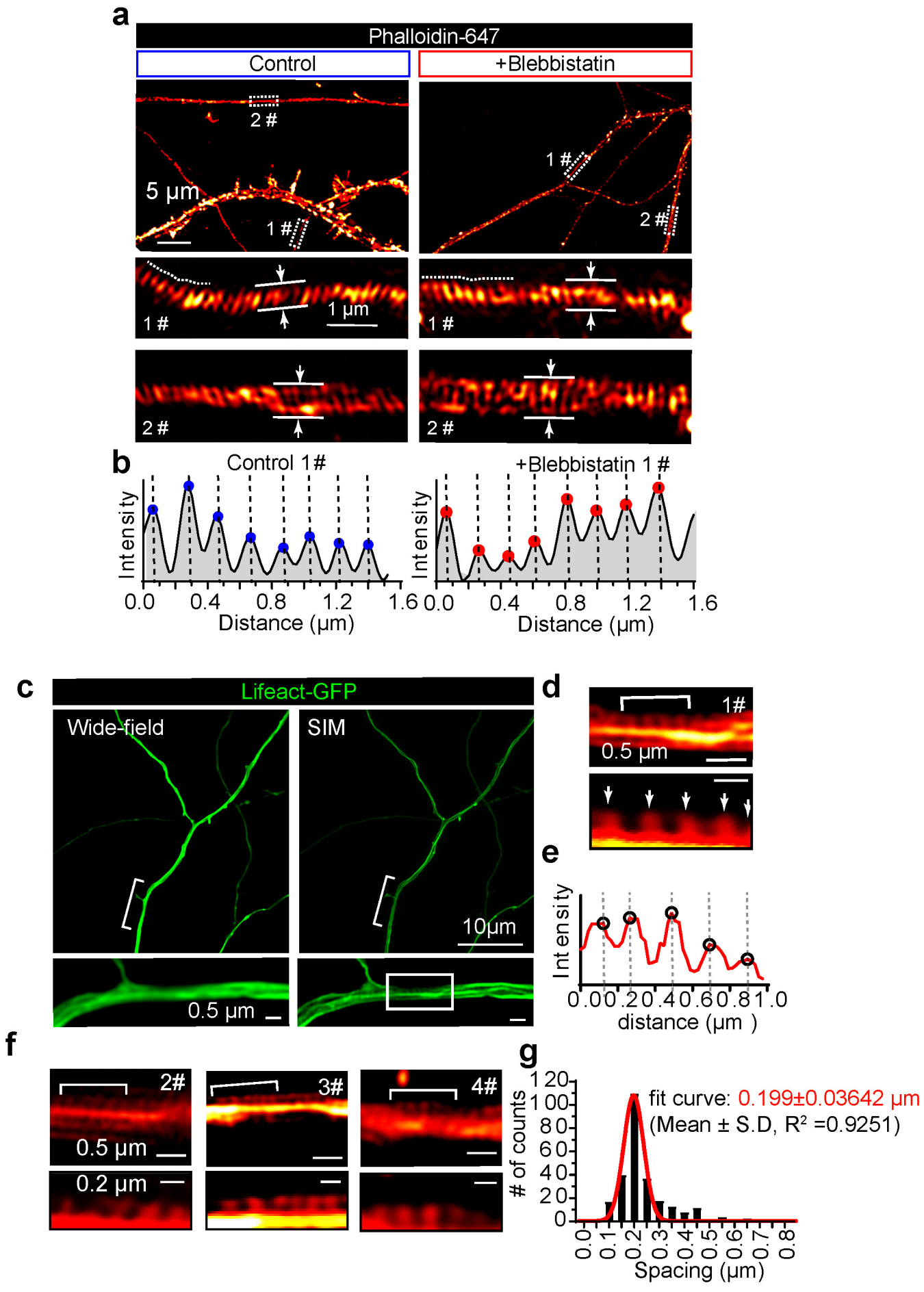

Supplementary Figure 2. Periodic distribution of F-actin rings along the axon of hippocampal neurons.

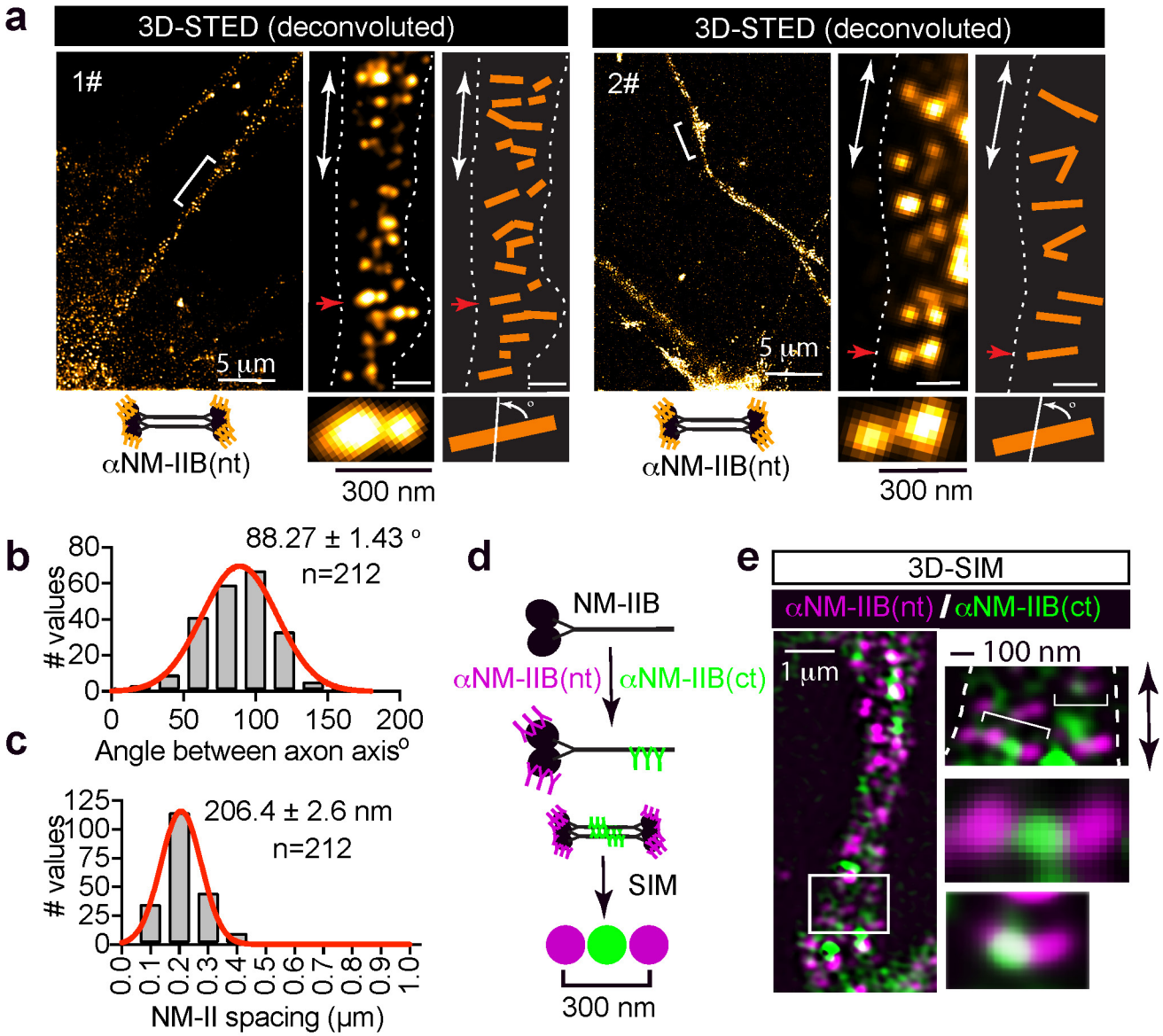

Supplementary Figure 3. Periodic NM-II filaments are perpendicular to the longitudinal axis of the axon.

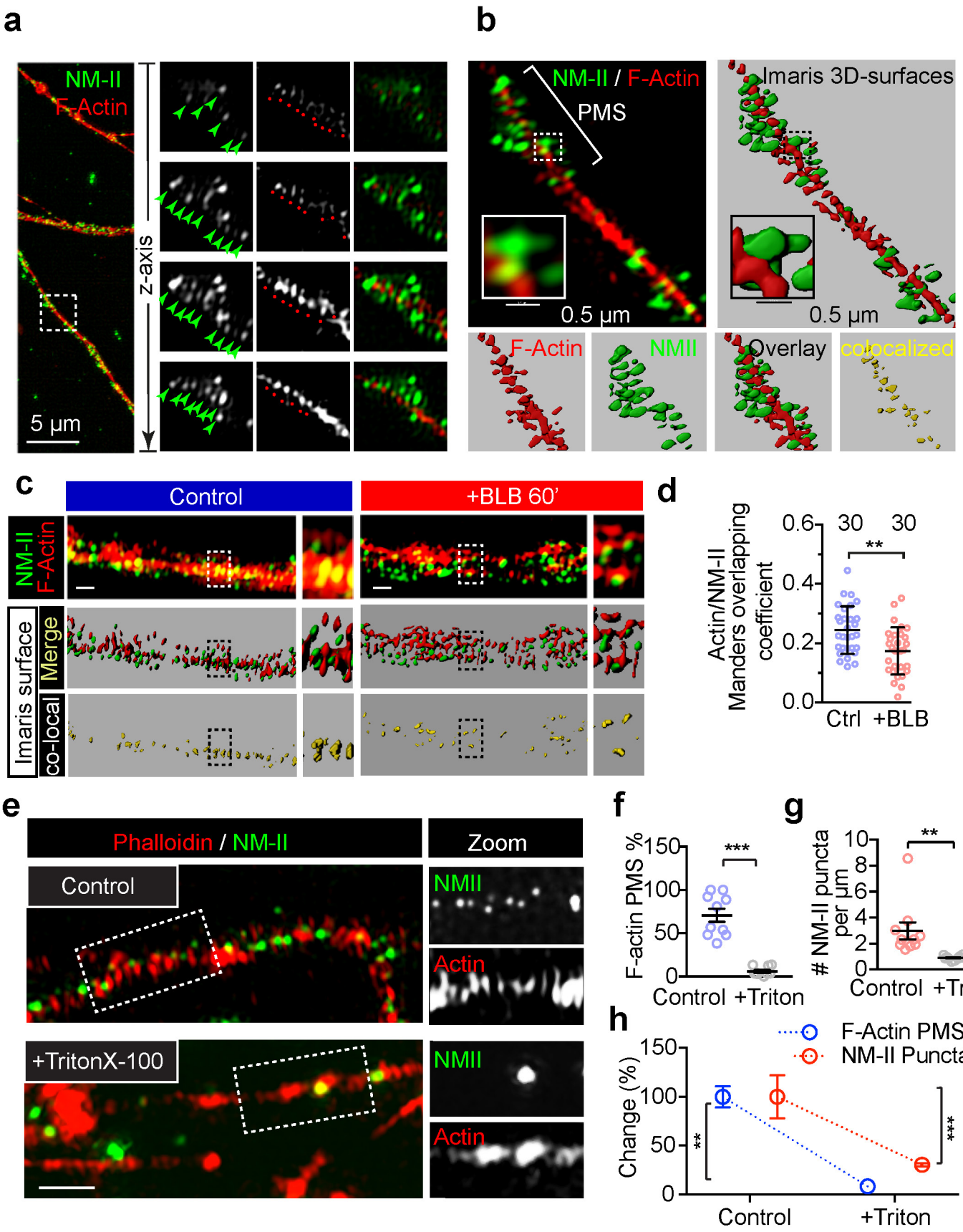

Supplementary Figure 4. NM-II immunostaining reveals a periodic pattern that correlates with the periodic actin rings along the axon.

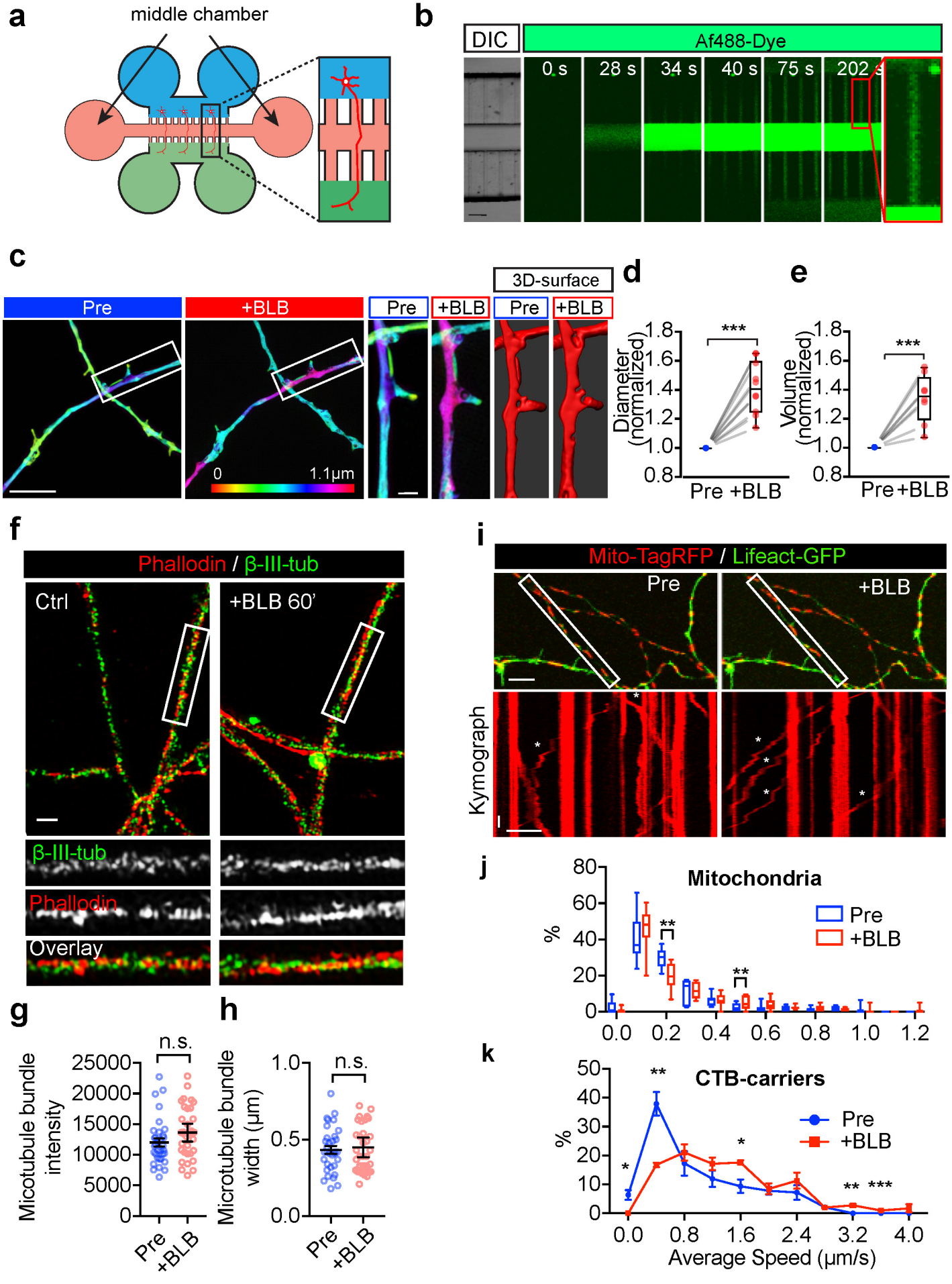

Supplementary Figure 5. Short-term inactivation of NM-II causes the axon diameter expansion without affecting the microtublue structure or docking mitochondria.